Chemical reactivity of thermal treated naturally occurring amphibole asbestos

Paolo Ballirano[1], Alessandro Pacella[1], Maura Tomatis[2,3], Francesco Turci[2,3], Cecilia Viti[4], and Andrea Bloise[5]

[1]Department of Earth Sciences, Sapienza University of Rome, Piazzale Aldo Moro 5, I-00185 Rome, Italy

[2]Department of Chemistry, University of Turin, Via P. Giuria 7, I-10125 Turin, Italy

[3]G. Scansetti" Center for Studies on Asbestos and Other Toxic Particulates, University of Turin, Italy

[4]Department of Physical, Geological and Environmental Sciences, University of Siena, Via Laterina 8, I-53100 Siena, Italy

[5]Department of Biology, Ecology and Earth Sciences, University of Calabria, I-87036 Arcavacata di Rende, CS, Italy

ABSTRACT

This study investigates the modification of the morphological and chemical-structural features of two amphibole asbestos, tremolite and crocidolite, occurring during thermal inertization. Amphiboles were heated at several temperatures that promoted iron oxidation, migration and/or clustering, and the formation of new crystalline and amorphous phases. The fibrous aspect of asbestos was preserved on recrystallization minerals and nanoparticles and amorphous phases were detected after treatment. The effects of the thermal modifications on the toxicologically relevant asbestos reactivity were evaluated by quantifying oxygen- and carbon-centred radical yields. Thermal treatments did not significantly alter carbon-centred radical yield, but they affected that of oxygen-centred radicals, namely •OH. At high-temperatures, structural breakdown of tremolite reduced the reactivity by sinking part of the reactive iron ions into the more stable TO_4 tetrahedra of the newly formed pyroxene(s). The breakdown of crocidolite induced the formation of Fe-rich phases, cristobalite and amorphous material that account for the restoration of radical reactivity. Our finding suggests that thermally inactivated asbestos and its breakdown products may still share some toxicologically relevant properties with pristine fibre and that asbestos inertization studies should consider other parameters, such as morphology and surface reactivity, beyond crystallinity when proving that a thermal treated asbestos-containing material is safe.

Keywords

Amphibole asbestos; inertization; free radical release; mineral reactivity; elongated mineral particles.

1. Introduction

The commercial term asbestos includes five fibrous amphiboles (actinolite, amosite, anthophyllite, crocidolite, and tremolite) and one fibrous serpentine mineral, chrysotile. Inhalation of asbestos fibres causes severe lung diseases (IARC, 2005) and asbestos use is banned in more than 50 countries (International Ban Asbestos Secretariat, 2016; Spasiano and Pirozzi, 2017). The industrial exploitation of asbestos and the fabrication of asbestos containing materials (ACMs) peaked in the 20th century, with a cumulative production of more than $2.1 \cdot 10^8$ tons of asbestos and more than three thousand types of products and consumer goods (Paglietti et al., 2012; Gualtieri, 2017). Among those, cement-asbestos has been –and in many countries still is– produced in large scale for the demand of construction industry. Cement asbestos is a composite material containing up to 20% of asbestos fibres embedded in a cement or polymeric matrix (Ross et al., 2008; Gualtieri, 2012). Amphibole asbestos, mainly crocidolite, is usually lower than 6% and chrysotile accounts for the rest (Gualtieri, 2012). The impressive quantity of cement asbestos installed worldwide requires extraordinary mitigation strategies. For instance, 30 and 15.5 million tons of ACMs, mainly as cement-asbestos roof tiles, are still installed in Italy and Poland, respectively (Plescia et al., 2003; Degiovanni et al., 2004; Witek and Kusiorowski, 2017) and deteriorated ACMs may release airborne or waterborne asbestos fibres and pose a risk to human health. As most of the cement-asbestos products have been installed in the second half of the 20th century, we are now getting closer to the end-of-life of ACMs. Currently, landfill disposal is the most adopted strategy to manage ACM end-of-life (Paolini et al., 2018). However, in search for a sustainable management of ACM end-of-life, the European Parliament proposes asbestos inertization, i.e. any treatment that induces a complete chemical structural transformation of asbestos, as a preferable way to landfilling (European Parliament resolution of 14 March 2013 on asbestos-related occupational health threats and prospects for abolishing all existing asbestos [2012/2065(INI)]). Several studies have recently investigated asbestos inertization, analysing and/or proposing thermal, thermochemical, biological, mechanical treatments (Turci et al., 2007; 2011a; Gualtieri et al., 2011; Kusiorowski et al., 2015a; Yamamoto et al., 2016; Spasiano, 2018; Bloise et al., 2018a; 2018b; 2019).

Among the various methods to promote the ACM inertization, thermal treatment with controlled recrystallization is currently one of the best available choice (Paolini et al., 2018). However, a full structure transformation may not always yield fully inert products. Newly formed mineral phases

might preserve reactivity and fibrous aspect of pristine asbestos minerals, and amorphous silica obtained during chrysotile inertization displayed a relevant surface reactivity in free radical generation and induced cytotoxic effect in cell culture (Gualtieri et al., 2019).

By following the thermally induced transformations of crocidolite and tremolite asbestos, this study aims at investigating the morphological and chemical structural features of amphibole asbestos during inertization and to give evidence of the coordinative and reactivity state of iron in the altered and newly formed crystalline phases. To this purpose, thermal treatment was used to induce structural modification on tremolite and crocidolite. These asbestos samples were chosen because they share a very similar structure (monoclinic *C*2/*m* amphiboles) and yet they exhibit a strongly different iron content (Deer et al., 2013). Notably, both the presence and the structural coordination of surface Fe are considered the main factors of fibre toxicity (Fubini et al., 1995), together with high aspect ratio (e.g., Stanton et al., 1981) and biopersistence (Van Oss et al., 1999).

It is known that thermal treatments of minerals induce two main modifications: a) at lower temperatures, surface oxidation and partial de-hydroxylation occurs, often accompanied by cation migration, while the crystalline phases of the pristine minerals are largely preserved; and b) a dramatic loss of crystalline structure followed by the appearance of newly formed mineral phase is achieved at higher temperature (Bloise et al., 2017a; 2017b). A detailed structural and morphological investigation of the altered minerals is here carried out, following a multi-technique approach (DSC, XRPD, SEM and TEM), and discussed at the light of pristine and altered mineral surface reactivity, by measuring oxygen- ($^{\bullet}OH$) and carbon-centred ($COO^{-\bullet}$) radicals, generated in cell-free tests (spin trapping/EPR).

2. Materials and methods

2.1. Asbestos minerals

A sample of tremolite from Maryland (USA), fully characterized from the crystal chemical and structural point of view by Pacella et al. (2010), was used in the present investigation. It has chemical formula $^{B}(Ca_{2.00}Mn_{0.02}Na_{0.01})_{\Sigma 2.03}{}^{C}(Mg_{4.48}Fe^{2+}_{0.44}Fe^{3+}_{0.08})_{\Sigma 5.00}{}^{T}[Si_{7.95}Al_{0.02}]_{\Sigma 7.97}O_{22}{}^{O3}[(OH)_{1.98}F_{0.01}]$. Fe^{2+} was found to be distributed over *M*(1), *M*(2) and *M*(3) sites of the octahedral layer, whereas Fe^{3+} was found only at *M*(2) site.

The well-known toxicological standard UICC crocidolite (fibrous riebeckite) was used and recently minero-chemically detailed by Pacella et al. (2019) and reported a chemical formula

$^{A}Na_{0.03}{}^{B}Na_{2.00}{}^{C}(Fe^{2+}_{2.21}Fe^{3+}_{2.04}Mg_{0.75})_{\Sigma 5.00}{}^{T}[Si_{7.95}Al_{0.02}]_{\Sigma 7.97}O_{22}{}^{O3}(OH)_{2}$

close to that of the end-member riebeckite. This formula is similar to that listed by Hodgson et al. (1965) for a sample, from the same locality, used by those authors to investigate the thermal

decomposition of crocidolite. Structural data indicated that both Fe^{2+} and Fe^{3+} are distributes over the *M*(1,2,3) sites exhibiting the following site-specific occupation preference: M(3)>M(1)>>M(2) and M(2)>>M(1)>M(3) for Fe^{2+} and Fe^{3+}, respectively.

2.2. DSC/TG

Differential Scanning Calorimetry (DSC) and Thermogravimetric Analysis (TG) were performed at the University of Calabria, Italy, in an alumina crucible under a constant aseptic air flow of 30 mL min^{-1} (oxidizing atmosphere) with a Netzsch STA 449 C Jupiter in a 30-1000°C (UICC crocidolite) and 30-1200°C (tremolite from Maryland) temperature range, with a heating rate of 10°C min^{-1} and a cooling rate of 20°C min^{-1}. Approximately 20 mg of sample was used for each run. Instrumental precision was checked by four repeated collections on a kaolinite reference sample revealing good reproducibility (instrumental theoretical T precision of ± 1.2°C), DSC detection limit < 1 μW. Derivative thermogravimetry (DTG), derivative differential scanning calorimetry (DDSC), onset, exo- and endo-thermic peaks were obtained using Netzsch Proteus thermal analysis software. About 200 mg of sample for each collection (previously gently ground in an agate mortar for 1 minute) were loaded into a 50-ml platinum crucible and heated within a vertical furnace equipped with Super Kanthal heating element (0–1700°C) with temperature controlled by PtRh–PtRh thermocouples (precision ±4°C). Tremolite and crocidolite were heated to 930°C and 1200°C, and to 650°C, 800 and 1000°C, respectively, in an oxidizing atmosphere with a heating rate of 10°C min^{-1}. Finally, the crucibles were cooled down to room temperature with a cooling rate of 20°C min^{-1} to investigate the transformation products *ex-situ* by X-ray powder diffraction (XRPD), Scanning and Transmission Electron Microscopy (SEM and TEM).

2.3. XRPD

XRPD data were acquired at Sapienza University of Rome, Italy, on a Bruker AXS D8 Advance equipped with incident-beam multilayer graded (Göbel) focussing mirrors and a PSD VÅntec-1. Samples were prepared as capillaries and measurements were performed in θ/θ transmission mode. Data were collected in the 5-145°2θ angular range, 0.022°2θ step size and 10 s counting time and analysed by the Rietveld method using Topas 6 (Bruker AXS, 2016) and the Fundamental Parameters Approach (FPA: Cheary and Coelho, 1992) to describe the peak shape. Coherently with the different morphology of the samples (see TEM and SEM sections of Results and discussion) an isotropic and an anisotropic broadening model were used to describe the peak shape of tremolite and crocidolite, respectively (Katerinopolou et al., 2012; Cametti et al., 2013; Ballirano et al., 2015). Absorption correction was modelled using the formalism of Sabine et al. (1998) and the

approach of Ballirano and Maras (2006) was adopted to handle the correlation between displacement parameters and absorption. Preferred orientation of amphiboles was modelled using spherical harmonics (4th-order, eight refinable parameters) by selecting the number of appropriate terms as suggested by Ballirano (2003). Parameters refined to small values as expected for samples prepared as capillaries. In order to obtain a fully consistent structural data set, the room temperature structure of tremolite was newly refined using the FPA, as in reference data a conventional approach for approximating the peak shape was used. Moreover, average bond distances < *M*(1)-O>, <*M*(2)-O>, and <*M*(3)-O> (and corresponding aggregate sizes of the constituent cations $<r^{M}>$) were not used to constrain the cation partition among those sites. Differently, in the present work the criteria for cation site assignment and indirect Fe^{2+}/Fe^{3+} partition of amphiboles were those described in Vignaroli et al. (2014). The list of reference starting structural data used in the various refinements is reported in Table S1.

2.4. SEM

SEM analysis was performed at the University of L'Aquila, Italy, using a Field Emission (FE) SEM Zeiss Gemini 500. Each sample was mounted on the stub with conductive carbon tape and a thin film (5 nm) of chromium was deposited on the sample surface using a Quorum Q 150T ES sputter in order to make it conductive for measurement purposes.

2.5. TEM

TEM analysis was performed on a JEOL JEM-2010 microscope at the University of Siena, Italy. The TEM was operated at 200 kV with a LaB_6 source and ultra-high-resolution pole pieces, resulting in a point resolution of 0.19 nm. The TEM is equipped with an energy dispersive spectrometer (EDS) Oxford ISIS and with an Olympus Tengra CCD camera (2k x 2k x 14 bit) for image acquisition. Pristine and heated samples have been dispersed on 200 mesh Cu-grids with holey carbon support film (two grids for each of the four samples) and subsequently carbon-coated.

2.6. Chemical reactivity

Chemical reactivity of both pristine and thermally treated samples was evaluated at the "G. Scansetti" Center, University of Turin, Italy, measuring the free radical generation by electron paramagnetic resonance (EPR) spectroscopy associated with the spin trapping technique, using 5,5'-dimethyl-1-pyrroline-1-oxide (DMPO, Cayman Chemical, Ann Arbor, Michigan, USA) as spin trapping agent. Asbestos fibres were suspended in a phosphate buffer solution (pH 7.4) containing DMPO and H_2O_2 or HCOONa as target molecules to detected hydroxyl or carboxyl radicals,

respectively. The release of the hydroxyl radical in the presence of hydrogen peroxide (He et al, 2013; Ensing et al., 2003) is held to occur *in vivo* when asbestos fibres are exposed to lysosomal fluids during alveolar macrophage phagocytosis, promoting a direct oxidative stress (Liu et al., 2013). The homolytic cleavage of the C-H bond in formate anion ($HCOO^-$) was employed as a model reaction that may occur to several biomolecules including peptides, proteins and lipids. Such a reaction yields the formation of a carbon-centred radical $COO^{-\bullet}$ and it was reported to be strongly dependent on the presence of poorly coordinated ferrous iron at the fibre surface (Turci et al., 2011b; Andreozzi et al., 2017). The suspensions were kept in the dark at 37°C and gently shaken. A fraction of the suspension was drawn after 10, 30, and 60 minutes, filtered through cellulose acetate (0.25 µm porosity) membranes and then transferred into a 50 µl-capillary tube for EPR measurement by means of Miniscope MS 100 spectrometer (Magnettech, Berlin, Germany). Instrument setting was: microwave power 10 mW; modulation 1000 mG; scan range 120 G; centre of field 3345 G. Blanks were performed in parallel in the absence of fibres. To quantify the amount of radical generated, each EPR spectrum was double-integrated and intensity is here reported in arbitrary unit as average value ± standard deviation. All experiments were repeated at least three times. The protocol for each test is described in detail below. All reagents were from Sigma-Aldrich, when not otherwise indicated.

$^{\bullet}OH$ generation test: the reaction tube contained 25 mg of sample, 500 µl of 0.5 M potassium phosphate buffer (pH 7.4) and 250 µl of 0.17 M DMPO. The reaction was triggered adding 250 µl of H_2O_2 (0.2 M).

$COO^{-\bullet}$ generation test: the reaction mixture contained 25 mg of sample, 250 µL of 0.17 M DMPO, and 250 µL of 60 mM ascorbic acid. The reaction was started by adding 500 µL of 2 M HCOONa solution in 1 M phosphate buffer.

3. Results and discussion

3.1. Alteration of fibrous amphiboles induced by thermal treatment

Thermal alterations of tremolite and crocidolite were investigated up to complete mineral breakdown by means of DSC and TG analysis. The DSC curve of the heated tremolite up to 1200°C is shown in Figure S1a. The wide endothermic peak centred at 1006°C was ascribed to tremolite breakdown even starting at 982°C (onset temperature) and ending at about 1030°C (end temperature), in agreement with the literature data (Bloise et al., 2017a; 2017b). The effect at 1030°C on derivative DSC (DDSC, Fig. S1a), due to the change of slope of the DSC curve, confirms the structural breakdown of tremolite before this temperature. Finally, the exothermic signal at 1052°C was assigned to the crystallization of pyroxenes and cristobalite (Johnson and Fegley, 2000; Bloise et al.,

2017b). The thermogravimetric analysis of tremolite (Fig. S1b) exhibited one main thermal event with a maximum mass loss (2.56 %, on TG curve) at 1016°C caused by tremolite dehydroxilation. In the 400-950°C range five downwardly events could be observed (inset in Fig. S2, @ 417, 574, 694, 779 and 870 °C) on DTG curve. They have been assigned to the dehydrogenation processes and to the progressive oxidation of ferrous iron in tremolite, before starting breakdown (@ 982°C). This interpretation was also confirmed by the effects on DDSC curve (inset in Fig. S1a) in the same temperature range (i.e., 400-950°C), that account for Fe oxidation. Our assignments are in line with the results of Wittels (1952) who thermographically recorded the oxidation of Fe^{2+} for ferrous-anthophyllite and hornblende at a temperature lower than their breakdown temperatures.

The DSC and TG analyses of the heated crocidolite up to 1000°C are reported in Fig. S1c and S1d, respectively. In the low temperature range (300-620°C), crocidolite exhibited four downwardly peaks recorder on DTG curve (330, 421, 486 and 613°C), assigned to the dehydrogenation processes, subsequently at which the iron oxidation occurs (Fig. S1d). Those assignments are confirmed by: i) the mass gain on TG curve (Fig. S1d); ii) the exothermic peaks on DSC curves due to the formation of an oxo-amphibole (partially dehydrogenated crocidolite). The Fe oxidation of crocidolite, in the range ca. 330-620°C, involves simultaneous oxidation of ferrous and hydroxyl ions leaving as product an oxo-amphibole. These findings are in agreement with results of Della Ventura et al. (2018). The reaction takes place on the surface and is dependent on the migration of protons and electrons through the crystal (Addison et al., 1962).

The endothermic peak at 919°C (Fig. S1c) is related to the breakdown of the structure which starts at about 800°C and ends at 930°C. The wide exothermic peak at 950°C is interpreted as crystallization to aegirine, cristobalite and hematite deriving from crocidolite breakdown (Hodgson et al., 1965; Kusiorowski, 2015b; Bloise et al., 2016b).

3.2. Morphological alterations induced by thermal treatments

Tremolite fibres showed the well-known acicular morphology of asbestos and were arranged in bundles (Fig. 1a). High-magnification image (inset) evidenced the polygonal cross section of individual fibrils, in agreement with previous observation by Pacella et al. (2015). After the thermal treatment at 1200°C fibrous morphology of the sample was well preserved (Fig. 1b). At higher magnification, however, the presence of newly formed sub-euhedral/euhedral crystals of nanometric size on the fibre surface could be observed (Fig. 1b, inset).

Crocidolite fibres appeared straight and rigid and arranged in thinner bundles than those formed by the tremolite sample (Fig. 1c). At higher magnification (inset), the bundles splitting into very thin fibrils with the typical nanometric diameter could be observed. As in the case of tremolite, crocidolite preserves the fibrous morphology after thermal treatment at 1000°C, even though the thermally modified fibres show very irregular edges, that account for a partial melting occurred during heating phase (Fig. 1d).

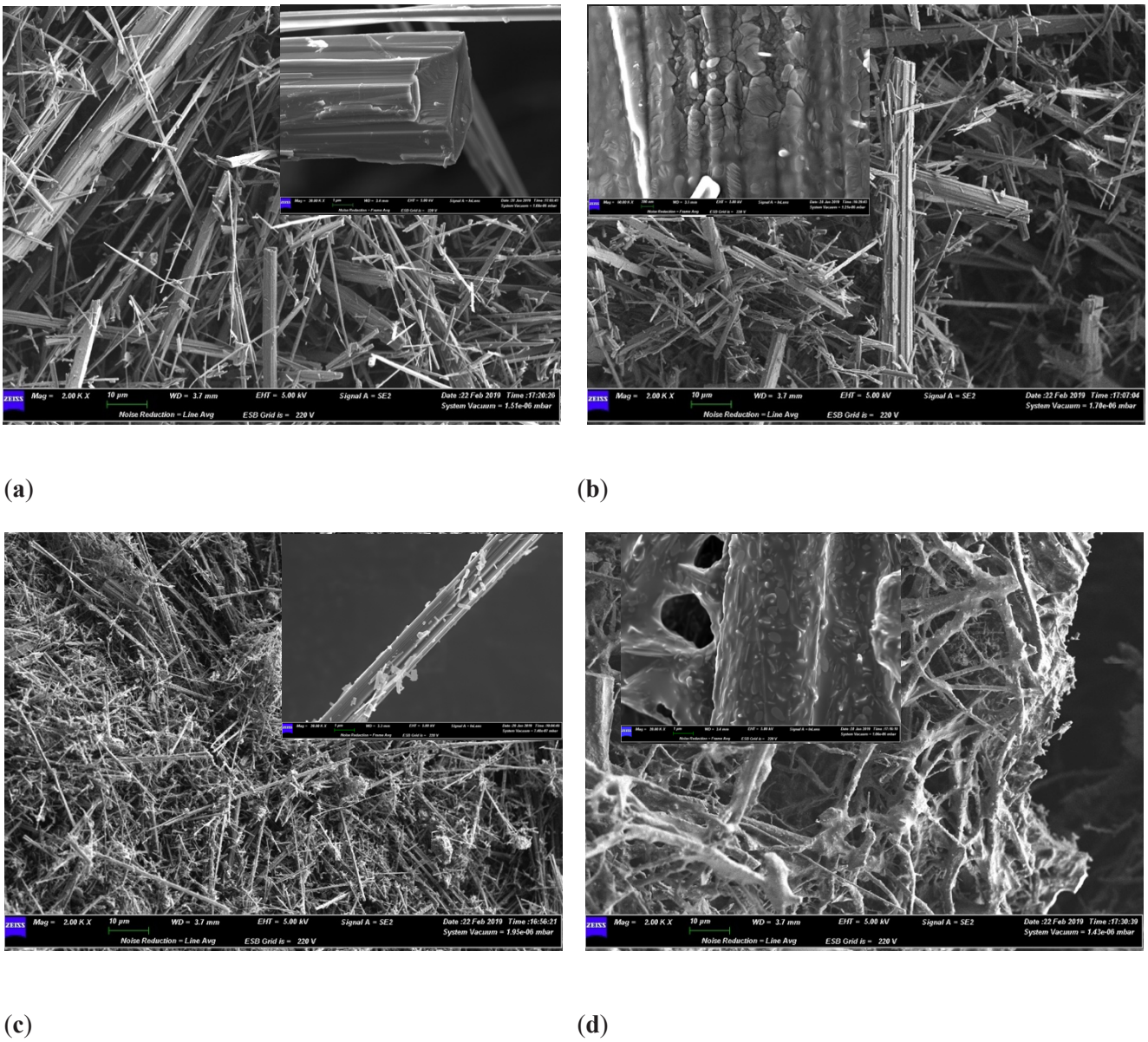

(**a**) (**b**)

(**c**) (**d**)

Fig. 1. FE-SEM image of tremolite pristine and heated at 1200°C (**a**) and (**b**) and crocidolite pristine and heated at 1000°C (**c**) and (**d**). Relative scale bars: low magnification, 10 μm; high magnification 1 μm (inset).

3.3. Structural modification induced by thermal treatments

XRPD analysis and Rietveld refinement on pristine and heated tremolite and crocidolite allowed to gain insight on the oxidative and structural situation of iron ions following thermal

treatment. Furthermore, XRPD allowed to quantify the neo-formed mineral phases. Cell parameters and volume of tremolite and crocidolite fibres and agreement factors of the Rietveld refinements are reported in Table S2, relevant bond distances (in Å) in Table S3 and Quantitative Phase Analysis (QPA) of the products of the breakdown are listed in Table 1. Conventional Rietveld plots of the analysed samples are shown in Fig. S2.

	Tremolite			Crocidolite				
Phases	RT P2010	1200°C	Idealized	RT P2019	650°C	800°C	1000°C	Idealized
Tremolite	100							
Crocidolite				93.51(13)	95.55(9)	72.4(7)		
Subcalcic diopside		69.9(3)	54.5					
Calcium-rich clinoenstatite		27.6(3)	37.9					
Aegirine				-	-	13.1(7)	21.1(11)	43.5
Cristobalite		2.33(5)	7.6			8.4(19)	24.0(4)	22.6
Quartz				1.51(3)	1.44(5)	1.63(6)	1.01(9)	
Hematite		0.20(2)			3.01(8)	4.43(11)	54.0(8)	33.8
Magnetite				1.90(4)				
Calcite				1.33(8)				
Siderite				1.26(8)				
Minnesotaite				0.48(6)				
Amophous*		minor				minor	abundant	

Table 1
Quantitative Phase Analysis (QPA) of the tremolite and crocidolite samples (wt.%). Room temperature data of Pacella et al. (2010) for tremolite (RT P2010) and Pacella et al. (2019) for crocidolite are also listed.
* Estimated from TEM images.

As expected, comparison with room temperature data of Pacella et al. (2010) indicates a slightly different iron content, Fe^{2+}/Fe^{3+} ratio and a corresponding Fe^{2+}/Fe^{3+} partition (Table S4) for tremolite. Those differences can be related to the common chemical variability exhibited by amphibole fibres (Andreozzi et al., 2009) and are consistent with the observed small differences between cell parameters and volume (Table S2) (Ballirano et al., 2017). Consistently with calorimetric data, XRPD of tremolite heated at 1200°C indicated that breakdown products consist of two pyroxenes, namely diopside-like and pigeonite-like, minor cristobalite and hematite traces the latter deriving from tremolite breakdown (Table 1).
Therefore, the corresponding idealized stoichiometric reaction of tremolite thermal breakdown is

$$Ca_2Mg_5[Si_8O_{22}](OH)_2 \xrightarrow{\Delta} 2\ CaMg[Si_2O_6] + 1.5\ Mg_2[Si_2O_6] + SiO_2 + H_2O\uparrow$$

The reaction does not take into account the iron content in tremolite (expected to be completely oxidized at the breakdown) and uses simplified compositions of both diopside-like and pigeonite-like

pyroxenes that, in effect, in order to preserve the overall chemical balance, should be more correctly classified as a subcalcic diopside and a calcium-rich clinoenstatite, respectively. This assignment is confirmed by the cell parameters of the two pyroxenes that are consistent with those of reference data (Table S5) for subcalcic diopside (McCallister et al., 1974) and pigeonite (Ohashi and Finger, 1974; Takeda et al., 1974), respectively. Notwithstanding these simplifications, the theoretical composition of the products of tremolite breakdown is in reasonable agreement with the QPA from Rietveld analysis (Table 1) and to TEM observations. Refinement of the s.s. at the M1 and M2 sites of both pyroxenes provided further confirmation to pyroxene classification. In fact, despite severe correlations existing among parameters (caused by two coexisting almost perfectly superimposed patterns) it was possible to retrieve, from the refined s.s., the chemical formula of the more abundant subcalcic diopside (accounting for ca. 70 wt.% of the mixture) which is $^{M2}(Ca_{0.674(10)}Mg_{0.326})_{\Sigma=1}{}^{M1}(Mg_{0.940(4)}Fe^{3+}{}_{0.060})^{T}[Si_{1.940(4)}Fe^{3+}{}_{0.060}O_6]$. As charge balance imposes a 1:1 partition of Fe^{3+} between M1 and T, the refinement has been restrained accordingly. Therefore, according to the refined s.s., part of Fe^{3+} of tremolite has been incorporated into the newly formed pyroxene structure coherently with the small amount of hematite observed in the mixture. In fact, 0.20 wt.% of Fe_2O_3 is one order of magnitude smaller than 4.50 wt.% $FeO_{tot.}$ reported by Pacella et al. (2010) in the chemical analysis by EPMA of tremolite from Maryland. The refined total of 0.12(1) Fe^{3+} apfu corresponds to ca. 4.5(4) wt.% Fe_2O_3 in agreement with the starting composition of tremolite. In his experimental work, Redhammer (1998) found that solubility of the ferri-Tschermak's (fts) molecule $CaFe^{3+}(Fe^{3+}Si)O_6$ in diopside reaches a maximum at T = 1150°C, very close to the present temperature of breakdown of tremolite, thus providing further support to the observed incorporation of Fe^{3+} into the subcalcic diopside structure.

In the case of the less abundant pigeonite (accounting for ca. 25 wt.% of the mixture) a significant increase of s.s. was observed at M2 confirming the onset of a Ca → Mg substitution scheme. According to the refined amount of Fe^{3+} in subcalcic diopside, only minor Fe^{3+}, if none, should enter pigeonite.

As expected, pristine tremolite observed at TEM consisted of long fibres, elongated along [001], showing fibrils with width ranging from a few tens of nm up to ca. 1 μm (Fig. 2a). At low magnification, the heated sample appeared very similar to pristine tremolite, with well-preserved fibrous habit and size (Fig. 2b). At higher magnification, we could observe fibrils that actually consisted of different phases, both crystalline and amorphous, thus indicating pseudomorphic transformations (e.g., Fig. 2c and 2d). In particular, tremolite fibres have been replaced by elongated pyroxene crystals and minor silica-rich amorphous material (px and amorph, respectively).

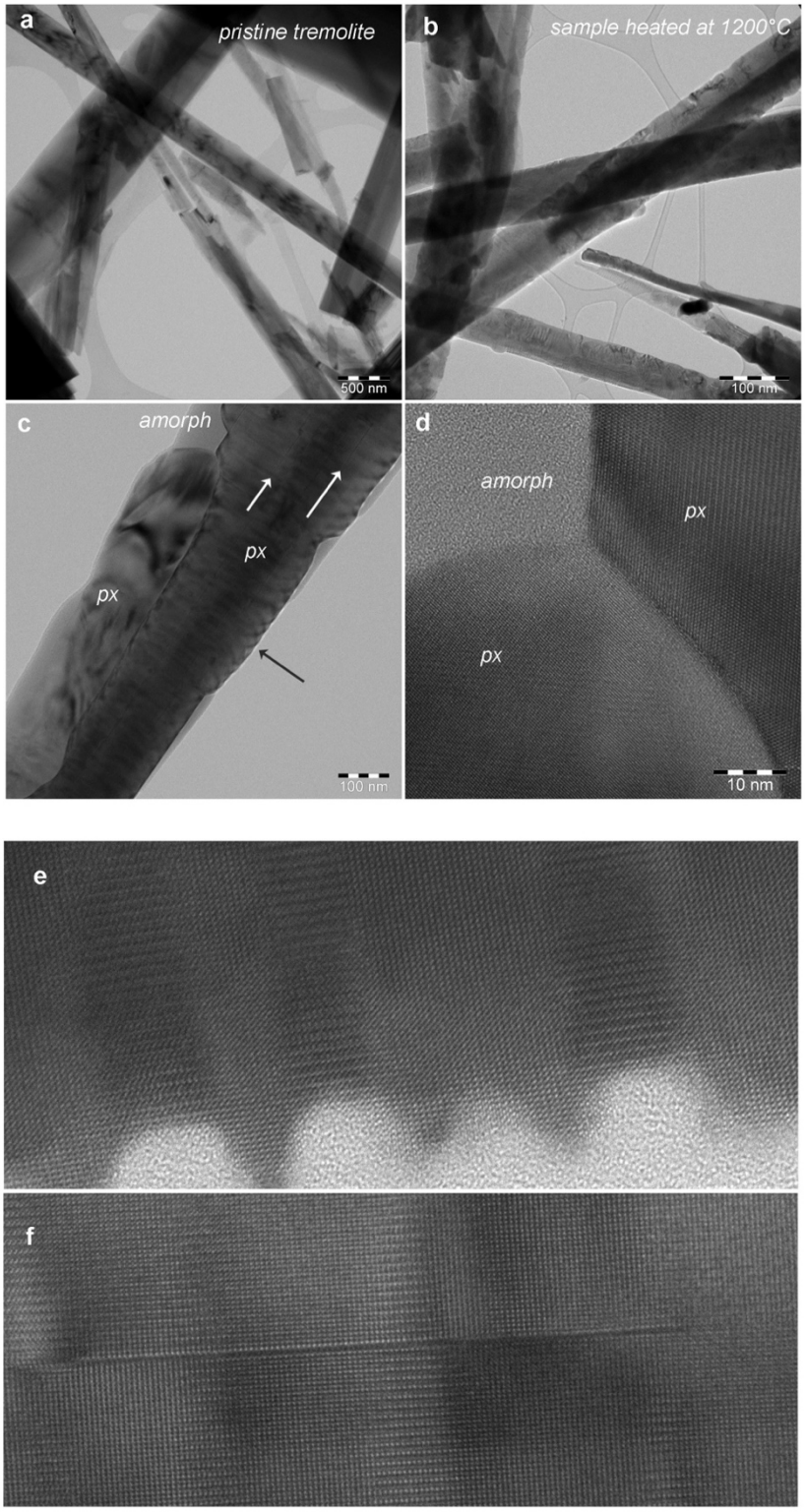

Fig. 2. TEM bright-field images of pristine tremolite (**a**) and heated at 1200°C sample (**b**-**f**). In (**c**) two pyroxene crystals (px), elongated along [001] but in different crystallographic orientation, are associated with amorphous material (amorph), preferentially occurring at the "fibre" boundaries; white arrows point to stacking faults, whereas the black arrow indicates the orientation of exsolution lamellae. (**d**) Detail showing pyroxene grains (px) in different crystallographic orientation, associated with amorphous material (amorph). High-resolution TEM images, showing exsolution lamellae (**e**), from 5 up to 20 nm wide, and a planar defect (f), possibly corresponding to a stacking fault, associated with exsolution lamellae.

Based on selected area electron diffraction (SAED) and high-resolution images (e.g., Figure 2d), pyroxene crystals are broadly elongated along their [001] axis, but are characterized by different crystallographic orientation, being variably rotated around [001]. Pyroxene crystals showed planar defects, corresponding to (100) stacking faults (white arrows in Figure 2c), and (001) exsolution lamellae (lamellar features parallel to the black arrow in Figure 2d). Fig. 2e and 2f show high-resolution images of exsolution lamellae and stacking faults, respectively. The width of exsolution lamellae ranges from 5 to 20 nm. The extremely low size of exsolution lamellae hampered the obtainment of pure EDS data of the two Ca-poor and Ca-rich pyroxenes, always giving rise to mixed analyses.

All those characteristics explain the persistence of the fibrous morphology and the relevant ε_0 microstrain broadening of the two pyroxenes observed from evaluation of the integral breadth of individual peaks in the Rietveld refinement, the latter required to accommodate the cell parameters misfit at their boundary. Cristobalite and hematite have not been detected in TEM grids of heated tremolite. This is not surprising, since it is probably the consequence of their low amount (2.47 and 0.26 wt.%, respectively, based on Rietveld data), coupled with the extremely small volume typically analysed in TEM samples.

UICC crocidolite thermal behaviour was analysed *ex-situ* at 650, 800 and 1000°C. Structure refinements show remarkable similarities with the results reported by Oberti et al. (2018) for riebeckite. In the case of the sample heated at 650°C the starting mixture, consisting of six phases, reduces to crocidolite, quartz and hematite (Table 1), the latter arising from magnetite oxidation and decomposition/oxidation of minnesotaite and siderite. Crocidolite cell parameters significantly contract as a result of iron oxidation and corresponding deprotonation (Table S2). This behaviour is confirmed by the shortening of the <*M*(1)-O> bond distance (Table S3) that indicates the prevailing onset of iron oxidation at this site which is coupled with a partial migration of Fe^{3+} from *M*(2). The increase of the s.s. at *M*(1) and the corresponding reduction at *M*(2) and *M*(3) indicate a redistribution of Mg from *M*(1) to *M*(2) and *M*(3) (Table 2). The constraint imposed by the starting content of Mg suggests that, at least at 650°C, the *M*(3) site is fully occupied. Na is partitioned between the *M*(4) and *A* sites that, for stabilizing the refinement, have been modelled as a single *A*(*m*) site. The Fe^{2+}/Fe^{3+} ratio passes from 1.06 at RT to 0.39 at 650°C clearly indicating the occurrence of extended iron oxidation. At 800°C, crocidolite starts to experience the breakdown as indicated by the formation of cristobalite and aegirine, as well as by an increase of the hematite content. Crocidolite cell parameters and volume increase approaching the values reported by Oberti et al. (2018) for the deprotonated sample 298KR-1301. Comparison with the sample heated at 650°C reveals the same s.s. at *M*(1) and a pronounced s.s. reduction (ca. 10%) at *M*(2). Both *M*(4) and *A*(*m*) show a minor increase of electron

density. The s.s. reduction at *M*(2) has been attributed to the almost complete segregation of Mg at that site. This fact testify the partial occupation of *M*(3) by Fe^{2+} and Fe^{3+} in perfect agreement with the findings of Oberti et al. (2018). The excess Fe^{2+} has been allocated at *M*(4) following Oberti et al. (2018).

Site	RT P2019	650°C	800°C	S2018	O2018 298KR
C					
M(1)	45.4(2)	50.0(3)	50.1(4)	49.88(8)	51.0(3)
M(2)	50.5(3)	48.6(3)	44.5(5)	50.44(9)	49.0(3)
M(3)	24.01(16)	22.34(19)	21.7(3)	25.13(6)	21.10(10)
$\Sigma_{M(1)+M(2)+M(3)}$	**119.9(7)**	**120.9(7)**	**116.2(12)**	**125.5(2)**	**121.1(7)**
B					
M(4)	21.2(2)	10.4(2)	10.9(4)	22.94(13)	17.6(3)
A	0.5(3)	8.49(14)	9.8(8)	1.75(11)	8.4(3)

	Fe^{2+}/Fe^{3+} partition from $<r^M>$		
Site	RT P2019	650°C	800°C
C			
M(1)	$[Mg_{0.47(2)}Fe^{3+}_{0.31}Fe^{2+}_{1.22}]$	$[Mg_{0.14(2)}Fe^{3+}_{1.82}Fe^{2+}_{0.04}]$	$[Mg_{0.14(3)}Fe^{3+}_{1.43}Fe^{2+}_{0.43}]$
M(2)	$[Mg_{0.11(1)}Fe^{3+}_{1.49}Fe^{2+}_{0.40}]$	$[Mg_{0.24(2)}Fe^{3+}_{1.13}Fe^{2+}_{0.63}]$	$[Mg_{0.54(4)}Fe^{3+}_{1.44}Fe^{2+}_{0.02}]$
M(3)	$[Mg_{0.14(1)}Fe^{3+}_{0.10}Fe^{2+}_{0.76}]$	$[Mg_{0.26(1)}Fe^{3+}_{0.18}Fe^{2+}_{0.56}]$	$[Fe^{3+}_{0.19}Fe^{2+}_{0.64}]$
$\Sigma_{M(1)+M(2)+M(3)}$	**$[Mg_{0.72(4)}Fe^{3+}_{1.90}Fe^{2+}_{2.38}]$**	**$[Mg_{0.64(5)}Fe^{3+}_{3.13}Fe^{2+}_{1.23}]$**	**$[Mg_{0.68(7)}Fe^{3+}_{3.07}Fe^{2+}_{1.08}]$**
Fe^{2+}/Fe^{3+}	1.06	0.39	0.39
B			
M(4)	$Na_{1.925(18)}$	$Na_{0.95(2)}$	$Fe^{2+}_{0.13}Na_{0.58}$
Am	$Na_{0.04(2)}$	$Na_{0.772(12)}$	$Na_{0.89(2)}$

Table 2
Site scattering (*s.s.*) at A, B and C sites from Rietveld refinement and Fe^{2+}/Fe^{3+} partition from $<r^M>$. For comparison purposes *s.s.* at A, B and C sites listed by Pacella et al (2019) for UICC crocidolite at RT (RT P2019), of Susta et al. (2018) for riebeckite (S2018) and of Oberti et al. (2018) for deprotonated riebeckite measured at RT (O2018 298KR) are reported.

XRPD indicated that crocidolite breakdown products are aegirine, hematite and cristobalite (Table 1) in substantial agreement with the findings of Vermaas (1952) and Patterson (1965). The corresponding idealized stoichiometric reaction is

$$Na_2Fe^{2+}_3Fe^{3+}_2[Si_8O_{22}](OH)_2 + 0.75\ O_2 \xrightarrow{\Delta} 1.5\ Fe_2O_3 + 2\ NaFe^{3+}[Si_2O_6] + 4\ SiO_2 + H_2O\uparrow$$

In this case, the theoretical composition of the products of crocidolite breakdown is in fair agreement with the QPA from Rietveld analysis (Table 1). In particular, hematite is significantly more abundant in the case of QPA than in the idealized reaction suggesting the occurrence of amorphous silicate phases other than the crystalline ones. It should be borne in mind that, in the present experimental set

up, the contribution of amorphous phases to the diffraction pattern is partly masked by that of the glass capillary and therefore their occurrence can be identified with difficulty. The small quantity of quartz arises from minor conversion of cristobalite at room temperature. It is worth noticing that cell parameters of the resulting cristobalite from the breakdown of the two amphiboles are larger than those of low-cristobalite (Table S6). This feature is more evident in the case of crocidolite breakdown products. Following Butler and Dyson (1997) they are similar to those of the so-called α' tetragonal form that has been attributed to a defect form of the α tetragonal form but having a constant quantity of defects/substituted cations which gives it a well-defined and consistent structure. In the case of crocidolite, the availability of large quantities of Na^{+} and Fe^{3+} seems to suggest their incorporation via the $Na^{+} + Fe^{3+} \rightarrow Si^{4+}$ substitution scheme.

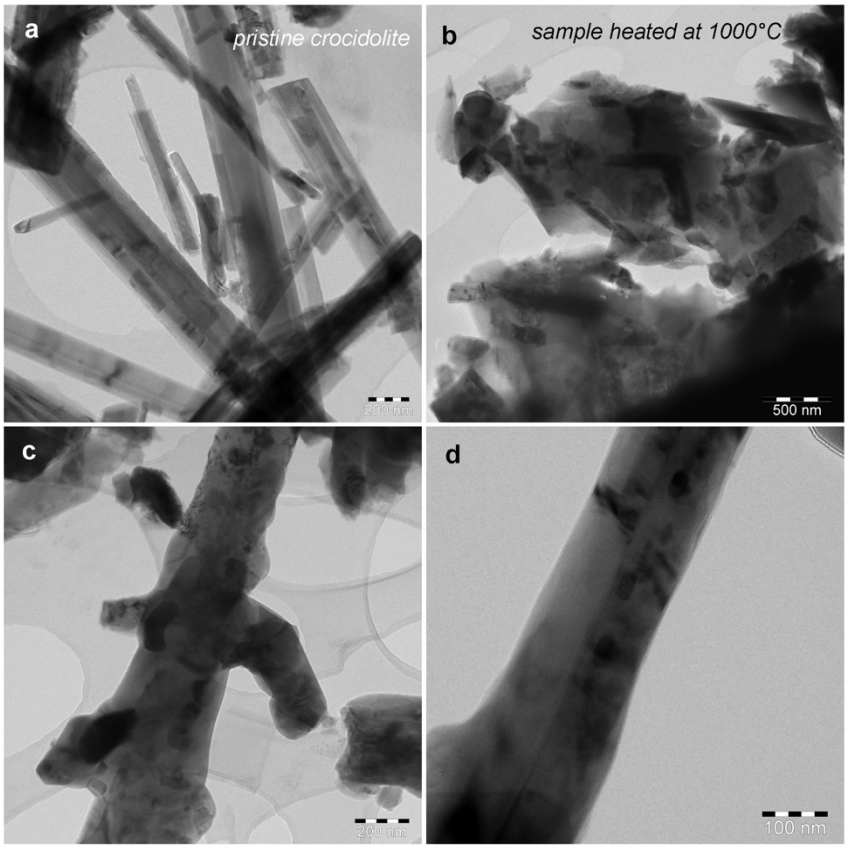

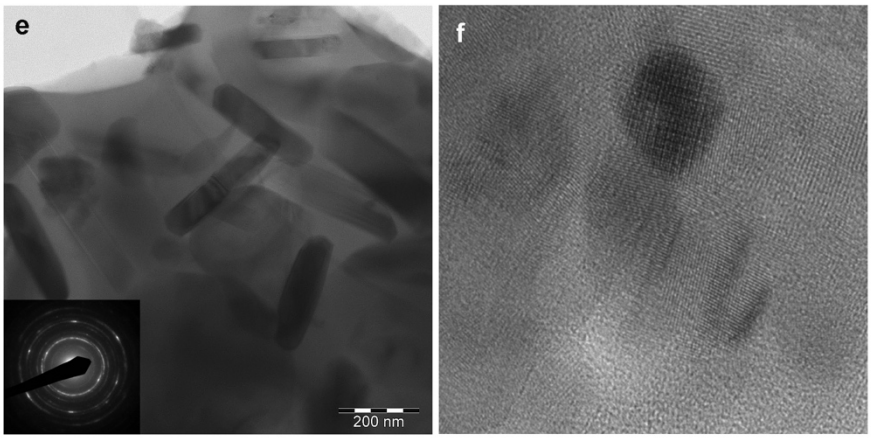

Fig. 3. TEM bright-field images of pristine crocidolite (**a**) and heated at 1000°C sample (**b**-**d**). (**b**) shows the typical nanotexture of the heated sample, with chaotic association of amorphous and different crystalline phases. (**c**) and (**d**) correspond to relatively rare examples of "fibrous" pseudomorphic aggregates. (**e**) Euhedral, rod-shaped hematite nanocrystals in random orientation, associated with an amorphous low contrast silicatic matrix; the inset shows the corresponding ring-shaped SAED pattern. (**f**) High-resolution image of the ultrafine association of different nanocrystals and amorphous phase; the size of the dark-contrast nanocrystal in the upper side is 8 nm.

Fig. 3a shows a representative TEM image of the pristine crocidolite sample consisting of several fibres of variable length and diameter. At difference from what observed in the case of heated tremolite, mostly consisting of "fibrous" pseudomorphs formed by elongated pyroxene crystals, the structure breakdown of the crocidolite sample produced a more complex nanogranular texture, where different phases, both amorphous and crystalline, are randomly associated (Fig. 3b). In some cases, fibrous pseudomorphs have also been observed (e.g., Fig. 3c and 3d), but also in these cases the newly formed phases form nanosized grains, with completely random crystallographic orientation, independent from the original crocidolite [001] fibre elongation. It is possible to hypothesize that the very gentle grinding of the sample in an agate mortar, prior to dispersion on the Cu-grid, may have favoured the almost complete destruction of the fibrous morphology, observed at the SEM, owing to the expected very low mechanical resistance and toughness of those aggregates.

The most evident and abundant crystals correspond to hematite, characterized by high contrast in TEM images, euhedral shape and crystal size typically greater than 200 nm (e.g., Fig. 3e). EDS analyses and SAED diffraction (for example, inset in Fig. 3e) confirm the presence of hematite. The low contrast matrix in Fig. 3f correspond to an amorphous, silica-rich phase in agreement with the results of QPA from XRPD. Pyroxene and cristobalite (21.1 and 24.0 wt.%, respectively from Rietveld data) are present in smaller nanocrystals, often less than 100 nm, and are finely associated with the amorphous silicate phase. This makes their identification more difficult. In fact, while it was possible to identify SAED patterns consistent with the presence of pyroxene, no patterns relating to cristobalite were found. It must be pointed out that the presence of iron centres trapped within the

large patches of amorphous material may be expected due the intimate association between amorphous material and crystalline phases. It is remarkable that crocidolite sample heated at 800°C is significantly different from that heated at 1000°C (Fig. 4). The fibrous habit is completely preserved until 800°C and corresponding SAED patterns show intense and sharp crocidolite reflections. Crocidolite fibres, however, are less regular and sharp with respect to the starting material, showing lobate fibre boundaries and locally heterogeneous TEM contrast. High-resolution images show that this feature is due to incipient reaction, preferentially occurring at fibre boundaries, and giving rise to amorphous material, hematite and, possibly, to ultrathin "slices" of pyroxene, in topotactic orientation.

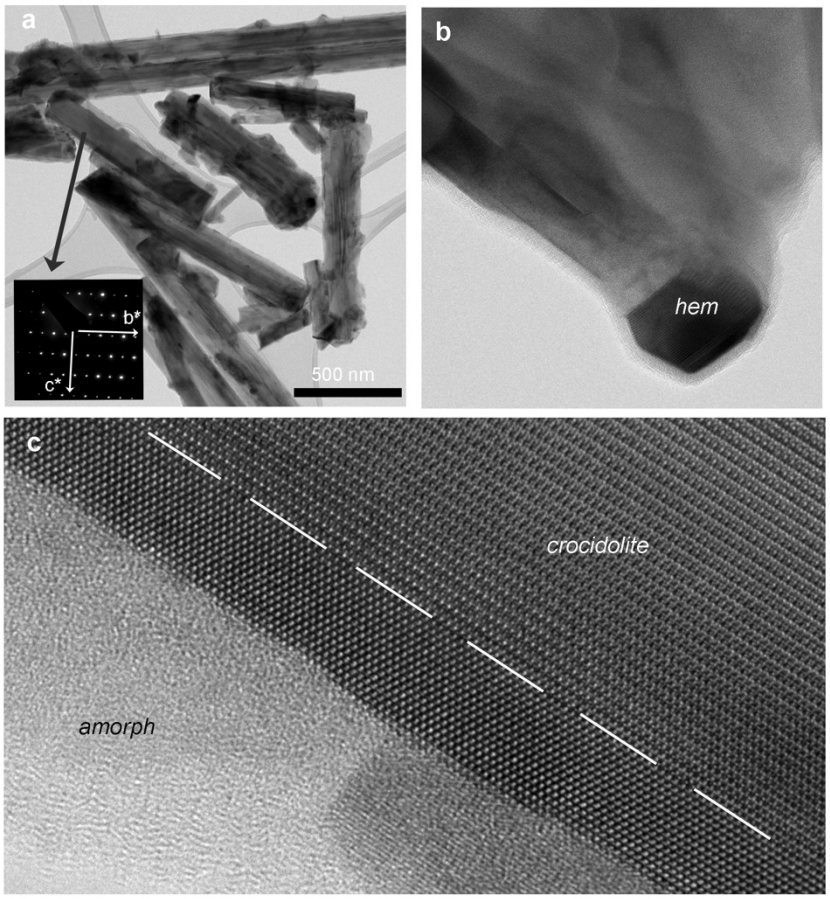

Fig. 4. TEM images corresponding to crocidolite sample heated at 800°C. (**a**) Crocidolite fibres in random orientation; the inset shows the *b*c** SAED pattern of one of the crocidolite fibres reported in the image (see arrow). Fibres have irregular, lobate boundaries. (**b**) Detail of the top boundary of a crocidolite fibre, showing incipient crystallization of hematite. (**c**) High-resolution image of the *b*c** crocidolite fibre shown in (**a**); the low contrast rim corresponds to amorphous material, possibly hosting newly formed nanocrystals (as the one in the lower side of the image). Dashed line highlights the sharp contact between crocidolite (inner fibre portion) and newly formed pyroxene (fibre rim).

3.4. Chemical reactivity of thermally altered fibrous amphiboles

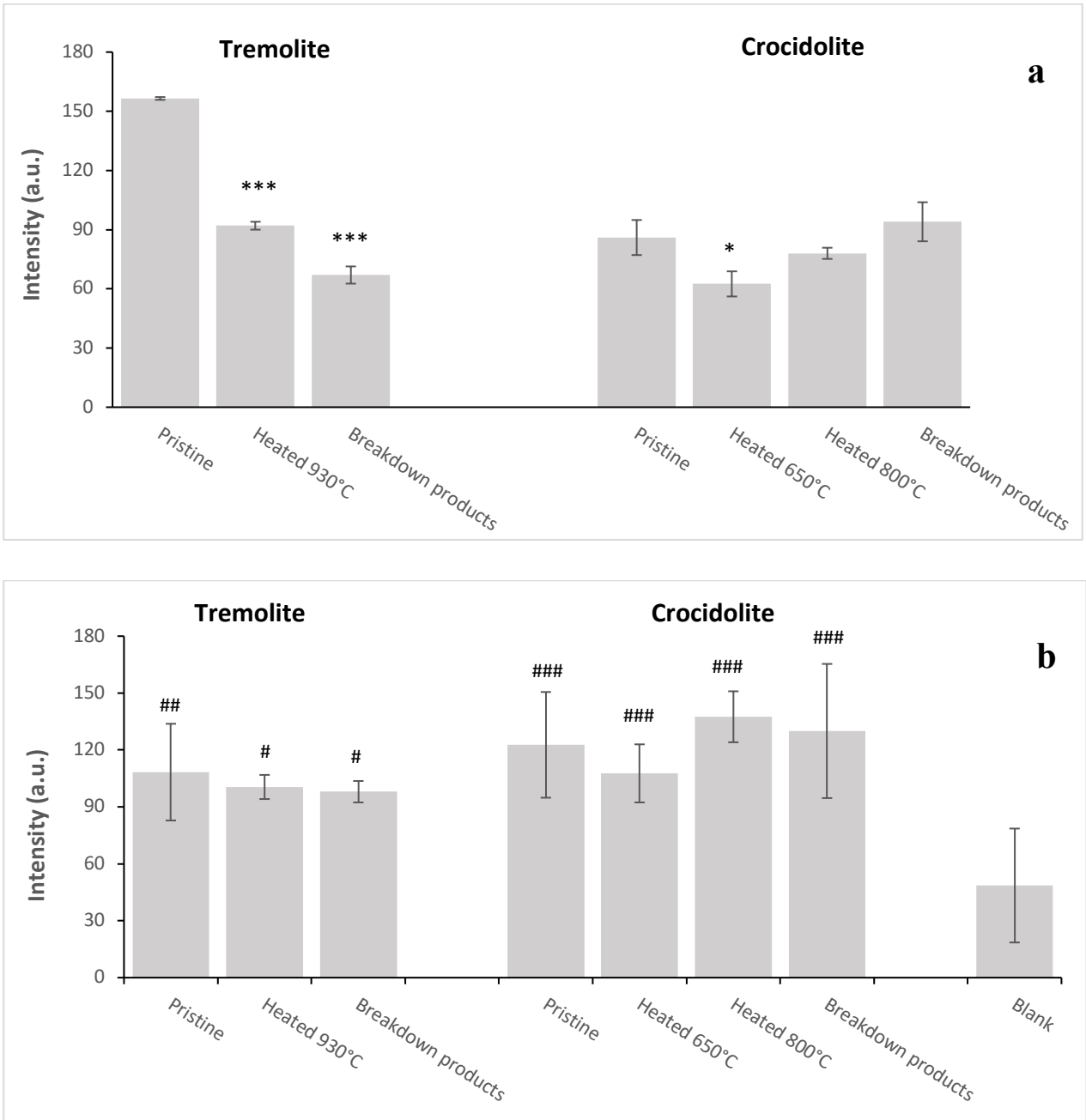

Fig. 5. Effect of thermal treatments on the amount of free radicals generated by Maryland tremolite and UICC crocidolite asbestos: EPR signal intensity of (**a**) [DMPO-OH]$^{\bullet}$ and (**b**) [DMPO-COO]$^{\bullet-}$ adducts detected before and after heating. Values reported refer to the maximum amount of radical generated by each sample. The intensity was obtained by double integration of EPR spectra and reported as means ± SD (for $^{\bullet}$OH: * $p<0.05$ and *** $p<0.001$ vs pristine sample; for $COO^{\bullet-}$: # $p<0.05$, ## $p<0.02$ and ### $p<0.01$ vs blank).

The radical surface reactivity of pristine and thermally altered amphiboles was quantified by means of two well-known tests, namely, the generation of oxygen- ($^{\bullet}$OH) and carbon-centred ($COO^{-\bullet}$) radicals. The former exploits the Fenton-like reactions, possibly assisted by a reductive Haber-

Weiss cycle, that occur when fibres are contacted with hydrogen peroxide. The latter investigates the reactivity of the mineral fibres towards a simple C-H bond, using formate anion as molecular probe. The test is sensitive to reduced iron and is carried out also in the presence of a biologically relevant reductant, namely ascorbic acid, which promotes reduction of ferric to the more reactive ferrous species (Turci et al., 2011b). The maximum amount (arbitrary unit) of the oxygen- and carbon-centred radical released by tremolite and crocidolite in pristine and thermally altered states are reported in Fig. 5a and 5b. Both pristine asbestos fibres showed a significant radical yield when reacted with hydrogen peroxide. The reactivity towards formate anion of pristine fibres was virtually absent (data not shown), but the reactivity was promptly restored upon reduction of the surface iron with ascorbic acid (Fig. 5b). The observed reactivation is explained, consistently-with previous works (Hardy and Aust, 1995; Fantauzzi et al., 2010), by the exposure of a large majority of ferric ions at the fibre surfaces. The comparison of the reactivity of the two pristine amphibole asbestos indicates that tremolite, in spite of its very low iron content, was more reactive in $^{\bullet}OH$ production (Fig. 5a) than crocidolite. However, $COO^{-\bullet}$ yield was similar in both amphiboles (Fig. 5b) and significantly higher that negative control (blank). This supports the hypothesis that the free-radical surface reactivity in asbestos is related neither to the total iron content, nor to the amount of iron on the surface, but it is due to specific iron sites in a well-defined coordination and oxidative state, as observed by some of us previously (Turci et al., 2011b; Andreozzi et al., 2017).

Thermal treatments inducing oxidation, iron migration and/or clustering, and formation of new phases did not significantly altered the $COO^{-\bullet}$ radical yields, in the presence of ascorbic acid. This is likely due to the occurrence, in all cases, of reducible surface ferric iron ions in a low-coordination state, as recently described (Andreozzi et al., 2017).

Conversely, thermal treatments altered the Fenton-like reactivity of the fibrous amphiboles. The reactivity of tremolite fibres heated at 930°C was significantly blunted, leading to a signal intensity about 40% lower than the pristine tremolite. This may be related to presence, on the fibre surface, of iron exclusively in form of Fe^{3+} centres. Such centres must be reduced to Fe^{2+} by Haber-Weiss cycle before they can react with hydrogen peroxide and yield $^{\bullet}HO$ radicals (Ensing et al., 2003; Turci et al., 2017). Interestingly, the breakdown products obtained by heating tremolite fibres to 1200°C showed a further reduction of the Fenton-like reactivity. The reduction of reactivity is compatible with the partial migration of Fe in the tetrahedral chain of pyroxene. Iron in tetrahedral coordination may not be available for reacting with H_2O_2 because of the stronger stability of the Fe-O bonds in tetrahedra and become inactive. On the other hand, the preserved reactivity may be due to the structural arrangement of pyroxene similar to that of amphibole (Fig 6), with Fe, hosted in the M1, rapidly

becoming exposed and reactive after the fast leaching of Ca^{2+} and Mg^{2+} cations present in the surface M2 sites.

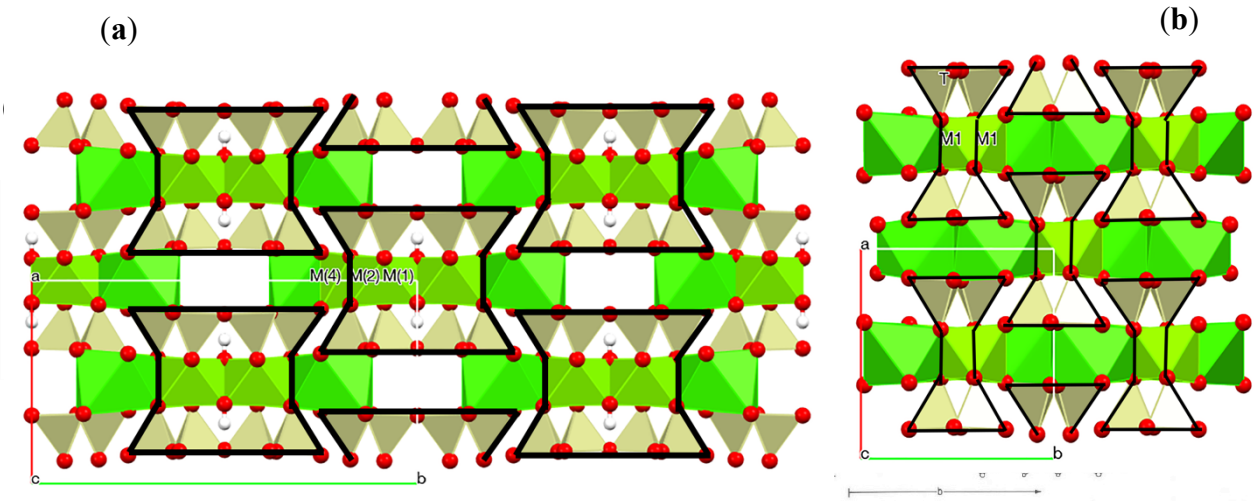

Fig. 6. (**a**) Projection along *c* of the structure of tremolite. Each area outlined in bold represents the so-called *I*-beam. This structural unit consists of a sandwich of couples of double chains linked by a strip of octahedra centred by *M*(2), *M*(1) and *M*(3) (inner, not shown) cations. The *M*(4)-centred square antiprism provides linking to neighbouring I-beams via 2 x *M*(4)-O(4), 2 x *M*(4)-O(5), and 2 x *M*(4)-O(6) bonds. The *A* sites, generally vacant, are located within the open space between base to base *I*-beams. (**b**) Projection along *c* of the structure of monoclinic pyroxene. Each shaded area represents the so-called *I*-beam. This structural unit consists of a sandwich of couples of single chains linked by a strip of octahedra centred by *M*1 cations. The *M*2 centred square antiprism provides linking to neighbouring *I*-beams.

The Fenton-like reactivity of crocidolite heated at 650 and 800°C resulted in more complex behaviour, due to the more complicated structural rearrangements that crocidolite is subjected to during thermal alteration. Heating up to 650°C promoted a significant reduction of Fenton-like reactivity, due to the strong oxidation of iron centres. Fe^{2+}/Fe^{3+} ratio is reduced from 1.06 to 0.39, in pristine and heated at 650°C sample, respectively (Table 2). The fibre reactivity was partially restored by treating crocidolite at 800°C. This can be explained by the incipient formation of new phases in the breakdown products (aegirine, cristobalite, hematite accounting for ca. 25 wt.%) and the migration of minor Fe^{2+} from the octahedral layer to the more external *M*(4) site of crocidolite relicts (see Fig. 6) (see Table 1 and 2, respectively). It is relevant to note that the preserved ability of oxidized crocidolite to promote Fenton-like reactions, is consistent with data reported by Otero-Areán et al. (2001), which showed that crocidolite heated in air at 800°C is still able to induce oxidative DNA strand breaks in presence of H_2O_2.

At 1000°C crocidolite is completely transformed, and breakdown products are responsible for the observed Fenton-like reactivity. To verify if the reactivity was compatible with the new mineral phases, namely hematite (54.0 %), cristobalite (24.0%), and aegirine (21.1%), each single phase was analysed for surface reactivity. Aegirine and hematite, but not cristobalite, yielded both oxygen- and

carbon-centred radicals (Fig S3), in agreement with previous results (Daniel et al., 1995; Huang et al., 2001). Fe-rich phases (aegirine and hematite) associated to form the nanogranular structure disclosed by TEM, likely account for the reactivity of the breakdown products of crocidolite. Specifically, the Fenton-like reactivity of aegirine stems from the presence of Fe^{3+} hosted in the *M*(1) site possibly exposed at the surface after leaching of Na^{+} from *M*(2). Cristobalite and other SiO_2 amorphous phases could exhibit some Fenton reactivity if traces of iron are present in the structure, as cell parameters of cristobalite and TEM analysis suggest. The presence of iron centres trapped within the large patches of amorphous material randomly associated with the crystalline phases could indeed significantly contribute to the overall radical reactivity of the breakdown products. These low-coordinated and well-dispersed iron centres are held to be very active in the radical production at the liquid-mineral interface (Pham et al., 2009; Turci et al., 2011b; Andreozzi et al., 2017).

4. Conclusions

This work shows that structural modifications which only involve iron oxidation are not sufficient to fully suppress the mineral reactivity. After thermal oxidation, tremolite and crocidolite were still able to generate carboxyl radicals in the presence of a reducing agent and their surface reactivity did not significantly differed from that of the pristine sample. Similarly, the hydroxyl radical yield from both amphiboles was reduced, but not suppressed, by thermal oxidation.

Our results highlight that, beside iron oxidation and coordination, surface reactivity of amphibole asbestos is driven by the lattice position of iron ions and that iron migration/partition during heating directly affects Fenton-like reactivity of mineral surface. Asbestos thermal decomposition produced new amorphous and crystalline phases, including Fe-bearing pyroxenes, that in some cases preserve asbestos fibrous habit and free-radical reactivity. On this basis, this work suggests that thermally inactivated asbestos may still share some toxicologically relevant properties with pristine fibre. It also recommends that asbestos inertization studies should consider other parameters, such as aspect ratio and surface reactivity, beyond crystallinity when proving that an asbestos-containing material is safe. Finally, this work suggests that fibrous pyroxenes and possibly other elongated mineral particles (EMP) that share with asbestos properties such as high aspect ratio and high surface reactivity, should be treated under precautionary principle and their health hazard should be carefully assessed.

Acknowledgements

This work was supported by MIUR PRIN 20173X8WA4.

References

Addison C.C., Addison W.E., Neal G.H., Sharp J.H. (1962) Amphiboles. Part I. The oxidation of crocidolite. J. Chem. Soc. 278, 1468–1471.

Addison J. and McConnell E.E. (2008) A review of carcinogenicity studies of asbestos and non-asbestos tremolite and other amphiboles. Regul. Toxicol. Pharmacol. 52, S187-S199

Andreozzi G.B., Ballirano P., Gianfagna A., Mazziotti-Tagliani S., Pacella A. (2009) Structural and spectroscopic characterization of a suite of fibrous amphiboles with high environmental and health relevance from Biancavilla (Sicily, Italy). Amer. Mineral. 94, 1333-1340.

Andreozzi G.B., Pacella A., Corazzari I., Tomatis M., Turci F. (2017) Surface reactivity of amphibole asbestos: a comparison between crocidolite and tremolite. Sci. Rep. 7, 14696.

Annex to the Resolution No. 39/2010 of the Council of Ministers; Programme for Asbestos Abatement in Poland 2009-2032; accepted by the Polish government on the 15 March 2010, Warsaw.

Ballirano P. (2003) Effects of the choice of different ionization level for scattering curves and correction for small preferred orientation in Rietveld refinement: the $MgAl_2O_4$ test case. J. Appl. Crystallogr. 36, 1056-1061.

Ballirano P., Bloise A., Gualtieri A.F., Lezzerini M., Pacella A., Perchiazzi N., Dogan M., Dogan A.U. (2017) The crystal structure of mineral fibres. In: A.F. Gualtieri (Ed.) "Mineral fibres: crystal chemistry, chemical–physical properties, biological interaction and toxicity". European Mineralogical Union, London, pp. 17-64.

Ballirano P. and Maras A. (2006) In-situ X-ray transmission powder diffraction study of the kinetics of the light induced alteration of realgar (α-As_4S_4). Eur. J. Mineral. 18, 589-599.

Ballirano P., Pacella A., Cremisini C., Nardi E., Fantauzzi M., Atzei D., Rossi A., Cametti G. (2015) Fe (II) segregation at a specific crystallographic site of fibrous erionite: A first step toward the understanding of the mechanisms inducing carcinogenicity. Micropor. Mesopor. Mat. 211, 49-63.

Baumann F., Buck B.J., Metcalf R.V., McLaurin B.T., Merkler D.J., Carbone M. (2015) The presence of asbestos in the natural environment is likely related to mesothelioma in young individuals and women from Southern Nevada. J. Thorac. Oncol. 10, 731-737

Bloise A., Punturo R., Catalano M., Miriello D., Cirrincione R. (2016a) Naturally occurring asbestos (NOA) in rock and soil and relation with human activities: the monitoring example of selected sites in Calabria (southern Italy). Ital. J. Geosci. 135, 268-279

Bloise A., Catalano M., Barrese E., Gualtieri A.F., Bursi Gandolfi N., Capella S., Belluso E. (2016b) TG/DSC study of the thermal behavior of hazardous mineral fibres. J. Therm. Anal. Calorim. 123, 2225-2239.

Bloise A., Catalano M., Critelli T., Apollaro C., Miriello D. (2017a) Naturally occurring asbestos: potential for human exposure, San Severino Lucano (Basilicata, Southern Italy). Environ. Earth Sci. 76, 648.

Bloise A., Kusiorowski R., Lassinantti Gualtieri M., Gualtieri A.F. (2017b) Thermal behaviour of mineral fibres. In: A.F. Gualtieri (Ed.) "Mineral fibres: crystal chemistry, chemical–physical properties, biological interaction and toxicity". European Mineralogical Union, London, pp. 215-252.

Bloise A., Catalano M., Gualtieri A. (2018a). Effect of grinding on chrysotile, amosite and crocidolite and implications for thermal treatment. Minerals 8, 135.

Bloise A., Kusiorowski R., Gualtieri A. (2018b). The effect of grinding on tremolite asbestos and anthophyllite asbestos. Minerals 8, 274.

Bloise A. (2019) Thermal behaviour of actinolite asbestos. J. Mater. Sci. 54, 11784-11795.

Bruker AXS (2016) Topas V6: General profile and structure analysis software for powder diffraction data. Bruker AXS, Karlsruhe, Germany.

Butler M.A and Dyson D.J. (1997) The quantification of different forms of cristobalite in devitrified alumino-silicate ceramic fibres. J. Appl. Crystallogr. 30, 467-475.

Cametti G., Pacella A., Mura F., Rossi M., Ballirano P., (2013) New morphological, chemical, and structural data of woolly erionite-Na from Durkee, Oregon, USA. Amer. Mineral. 98, 2155-2163.

Cheary R.W. and Coelho A.A. (1992) A Fundamental Parameters Approach of X-ray line-profile fitting. J. Appl. Crystallogr. 25, 109-121.

Clark J.R., Ross M., Appleman, D.E. (1971) Crystal chemistry of a lunar pigeonite. Amer. Mineral. 56, 888-906.

Daniel L. N., Mao Y., Wang T. C. L., Markey C. J., Markey S. P., Shi X. L., Saffiotti U. (1995). DNA strand breakage, thymine glycol production, and hydroxyl radical generation induced by different samples of crystalline silica in vitro. Environ. Res., 71(1), 60-73

Deer W., Howie R.A., Zussman J. (2013) An Introduction to the Rock-forming Minerals. London: Mineralogical Society, - Rock-forming Minerals 498 pages

Degiovanni D., Pesce B., Pondrano N. (2004) Asbestos in Italy. Int. J. Occup. Environ. Health 10, 193-197.

Della Ventura G., Mihailova B., Susta U., Guidi M. C., Marcelli A., Schlüter J., Oberti R. (2018) The dynamics of Fe oxydation in riebeckite: a model for amphiboles, Amer. Mineral., 2018, 103, 1103–1111.

Downs R.T. and Palmer D.C. (1994) The pressure behavior of α cristobalite. Amer. Mineral. 79, 9-14.

Ensing B., Buda F., Baerends, E. J. (2003) Fenton-like chemistry in water: Oxidation catalysis by Fe(III) and H_2O_2. J. Phys. Chem. A 107, 5722–5731.

European Parliament resolution of 14 March 2013 on asbestos-related occupational health threats and prospects for abolishing all existing asbestos [2012/2065(INI)]. Strasbourg: European Parliament.

Fantauzzi M., Pacella A., Atzei D., Gianfagna A., Andreozzi G., Rossi A. (2010) Combined use of X-ray photoelectron and Mossbauer spectroscopic techniques in the analytical characterization of iron oxidation state in amphibole asbestos. Anal. Bioanal. Chem. 396, 2889–2898.

Finger L.W and Hazen R.M. (1980) Crystal structure and isothermal compression of Fe_2O_3, Cr_2O_3, and V_2O_3 to 50 kbars. J. Appl. Phys. 51, 5362-5367.

Fubini B., Mollo L., Giamello, E. (1995) Free radical generation at the solid/liquid interface in iron containing minerals. Free Radical Res. 23, 593-614.

Gualtieri A.F., Giacobbe C., Sardisco L., Saraceno M., Gualtieri M.L., Lusvardi G., Cavenati C., Zanatto I. (2011) Recycling of the product of thermal inertization of cement-asbestos for various industrial applications. Waste Manag. 31, 91-100.

Gualtieri A.F. (2012) Mineral fibre-based building materials and their health hazards. In: F. Pacheco-Torgal, S. Jalali, A. Fucic (Eds.) “Toxicity of Building Materials”. Woodhead Publishing, pp. 166-195.

Gualtieri A.F. (2017) Introduction. In: A.F. Gualtieri (Ed.) “Mineral fibres: crystal chemistry, chemical–physical properties, biological interaction and toxicity”. European Mineralogical Union, London, pp. 1-15.

Gualtieri A.F., Lusvardi G., Zoboli A., Di Giuseppe D., Lassinantti Gualtieri M. (2019) Biodurability and release of metals during the dissolution of chrysotile, crocidolite and fibrous erionite. Environ Res., 171, 550-557.

Hardy J.A. and Aust A.E. (1995) Iron in asbestos chemistry and carcinogenicity. Chem. Rev. 95, 97-118.

Harper M. (2008) 10th anniversary critical review: naturally occurring asbestos. J. Environ. Monit. 10, 1394-1408.

Hawthorne F.C. and Oberti R. (2007) Amphiboles: Crystal chemistry: In: F.C. Hawthorne, R. Oberti, G. Della Ventura, A. Mottana (Eds) "Amphiboles: Crystal chemistry, occurrence, and health issues". Reviews in Mineralogy and Geochemistry, vol. 67, Mineralogical Society of America, Chantilly, VA, USA, pp. 1-54.

He, J., Yang, X., Men, B., & Wang, D. (2016). Interfacial mechanisms of heterogeneous Fenton reactions catalyzed by iron-based materials: A review. J. Environ. Sci., 39, 97-109.

Hodgson J.T. and Darnton A. (2000) The quantitative risks of mesothelioma and lung cancer in relation to asbestos exposure. Ann. Occup. Hyg. 44, 565-601.

Hodgson A.A., Freeman A.G., Taylor H.F.W. (1965) The thermal decomposition of crocidolite from Koegas, South Africa. Mineral Mag. 35, 5-30.

Huang H.H., Lu M.C. and Chen J.N. (2001) Catalytic decomposition of hydrogen peroxide and 2-chlorophenol with iron oxides. Wat. Res., 35, 2291-2299.

IARC (2005). Report of the Advisory Group to Recommend Updates to the Preamble to the IARC Monographs (IARC Int. Rep. No. 05/001).

International Ban Asbestos Secretariat. <http://ibasecretariat.org/lka_alpha_asb_ban_280704.php, 2016> (accessed 19.12.16).

Johnson N.M. and Fegley B., Jr. (2000) Water on Venus: New insights from tremolite decomposition. Icarus 146, 301-306.

Kashimura K., Yamaguchi T., Sato M., Yoneda S., Kishima T., Horikoshi S., Yoshikawa N., Mitani T., Shinohara N. (2015) Rapid transformation of asbestos into harmless waste by a microwave rotary furnace: application of microwave heating to rubble processing of the 2011 Tohoku earthquake. J. Hazard Toxic Radioact. Waste 19, 04014041-04014048.

Katerinopoulou A., Balic-Zunic T., Lundegaard L.F. (2012) Application of the ellipsoid modeling of the average shape of nanosized crystallites in powder diffraction. J. Appl. Crystallogr. 45, 22–27.

Kleinfeld M.M.D., Messite J.M.D., Zaki, M.H.M.D. (1974) Mortality experiences among talc workers: A follow-up study. J. Occup. Med. 16, 345-349.

Kusiorowski R., Zaremba T., Piotrowski J., Podwórny J. (2015a) Utilisation of cement-asbestos wastes by thermal treatment and the potential possibility use of obtained product for the clinker bricks manufacture. J. Mater. Sci. 50, 6757-6767.

Kusiorowski R., Zaremba T., Gerle A., Piotrowski J., Simka W., Adamek J. (2015b) Study on the thermal decomposition of crocidolite asbestos. J. Therm. Anal. Calorim. 120, 1585-1595.

Le Page Y. and Donnay G. (1976) Refinement of the crystal structure of low-quartz. Acta Cryst. B32, 2456-2459.

Liu, G., Cheresh, P., & Kamp, D. W. (2013). Molecular basis of asbestos-induced lung disease. Annu. Rev. Pathol-Mech. Dis. 8, 161-187

McCallister R.H., Finger L.W., Ohashi Y. (1974) Refinement of the crystal structure of a subcalcic diopside. Carnegie Inst. Washington Year Book 73, 518-522.

Oberti R., Boiocchi M., Zema M., Hawthorne F.C., Redhammer G.J., Susta U., Della Ventura G. (2018) The high-temperature behaviour of riebeckite: expansivity, deprotonation, selective Fe oxidation and a novel cation disordering scheme for amphiboles. Eur. J. Mineral. 30, 437-449.

Ohashi Y. and Finger L.W. (1974) A lunar pigeonite: crystal structure of primitive cells domains. Carnegie Inst. Washington Year Book 73, 525-531.

Otero Areán C., Barceló F., Fenoglio I., Fubini B., Llabrés i Xamena F.X., Tomatis M. (2001) Free radical activity of natural and heat treated amphibole asbestos. Inorg. Biochem., 83, 211-216.

Pacella A., Andreozzi G.B., Fournier J. (2010) Detailed crystal chemistry and iron topochemistry of asbestos occurring in its natural setting. A first step to understand its chemical reactivity. Chem. Geol. 277, 197-206.

Pacella A., Fantauzzi M., Turci F., Cremisini C., Montereali M.R., Nardi E., Atzei D., Rossi A., Andreozzi G.B. (2015) Surface alteration mechanism and topochemistry of iron in tremolite asbestos: a step toward understanding the potential hazard of amphibole asbestos. Chem Geol., 405, 28–38.

Pacella A., Andreozzi G.B., Corazzari I., Tomatis M., Turci F. (2018) Surface reactivity of amphibole asbestos: A comparison between two tremolite samples with different surface area. Period. Mineral., 87, 195-205.

Pacella A., Andreozzi G.B., Nodari L., Ballirano P. (2019) Chemical and structural characterization of UICC crocidolite fibres from Koegas Mine, Northern Cape (South Africa). Period. Mineral. 88, 297-306.

Paglietti F., Malinconico S., Di Molfetta V., Bellagamba S., Damiani F., Gennari F., De Simone P., Sallusti F., Giangrasso M. (2012) Asbestos risk: from raw material to waste management: the Italian experience. Crit. Rev. Env. Sci. Tec. 42, 1781-1861.

Paolini V., Tomassetti L., Segreto M., Borin D., Liotta F., Torre M., Petracchini F. (2019) Asbestos treatment technologies. J. Mater. Cycles Waste Manag. 21, 205-226.

Patterson J.H. (1965) The thermal disintegration of crocidolite in air and in vacuum. Mineral Mag. 35, 31-37.

Patterson J.H. and O'Connor D.J. (1966) Chemical studies of amphibole asbestos. I. Structural changes of heat-treated crocidolite, amosite, and tremolite from infrared absorption studies. Aust. J. Chem. 19, 1155-1164.

Perkins R.A., Hargesheimer J., Fourie W. (2007) Asbestos release from whole building demolition of buildings with asbestos-containing material. J. Occup. Environ. Hyg. 4, 889-894.

Pham A.L.T., Lee C., Doyle F.M., Sedlak D.L. (2009). A Silica-Supported Iron Oxide Catalyst Capable of Activating Hydrogen Peroxide at Neutral pH Values. Environ. Sci. Technol. 43, 8930-8935.

Plescia P., Gizzi D., Benedetti S., Camillucci L., Fanizza C., De Simone P., Paglietti F. (2003) Mechanochemical treatment to recycling asbestos-containing waste. Waste Manage. 23, 209-218.

Redhammer G.J. (1998) Mössbauer spectroscopy and Rietveld refinement on synthetic ferri-Tschermak's molecule $CaFe^{3+}(Fe^{3+}Si)O_6$ substituted diopside. Eur. J. Mineral. 10, 439-452.

Redhammer G.J., Amthauer G., Roth G., Tippelt G., Lottermoser W. (2006) Single crystal X-ray diffraction and temperature dependent ^{57}Fe Mössbauer spectroscopy on the hedenbergite-aegirine $(Ca,Na)(Fe^{2+},Fe^{3+})Si_2O_6$ solid solution. Amer. Mineral. 91, 1271-1292.

Roggli V.L. and Coin P. (2004) Mineralogy of asbestos. In: V. Roggli and T.D. Oury (Eds.) "Pathology of Asbestos Associated Diseases". Springer Verlag: New York, NY, USA, pp. 1-17.

Ross M., Langer A.M., Nord G.L., Nolan R.P., Lee R.J., Van Orden D., Addison J. (2008) The mineral nature of asbestos. Regulatory Toxicology and Pharmacology 52(S1), S26-S30.

Ross M., Smith W.L., Ashton W.H. (1968) Triclinic talc and associated amphiboles from Gouverneur mining district New York. Am. Mineral. 53, 751-769.

Sabine T.M., Hunter B.A., Sabine W.R., Ball C.J. (1998) Analytical expressions for the transmission factor and peak shift in absorbing cylindrical specimens. J. Appl. Crystallogr. 31, 47-51.

Spasiano D. and Pirozzi F. (2017) Treatments of asbestos containing wastes. J. Environ. Manag. 204, 82-91.

Spasiano D. (2018) Dark fermentation process as pretreatment for a sustainable denaturation of asbestos containing wastes. J. Haz. Mater. 349, 45-50.

Stanton M.F., Layard M., Tegeris A., Miller E., May M., Morgan E., Smith A. (1981). Relation of particle dimension to carcinogenicity in amphibole asbestoses and other fibrous minerals. J. Natl Cancer Inst. 67, 965–975.

Susta U., Della Ventura G., Hawthorne F.C., Abdu Y.A., Day M.C., Mihailova B., Oberti R. (2018) The crystal-chemistry of riebeckite, ideally $Na_2Fe^{2+}{}_3Fe^{3+}{}_2Si_8O_{22}(OH)_2$: a multi-technique study. Mineral. Mag. 82, 837-852.

Takeda H., Miyamoto M., Reid A.M. (1974) Crystal chemical control of element partitioning for coexisting chromite-ulvospinel and pigeonite-augite in lunar rocks. Proc. 5th Lunar Sci. Conf. 1, 727-741.

The European Parliament and the Council of the European Union. Directive 2003/18/EC of the European Parliament and of the Council of 27 March 2003 amending Council Directive 83/477/EEC on the protection of workers from the risks related to exposure to asbestos at work. Off. J. Eur. Union 2003, L97, 48-52.

Turci F., Tomatis M., Mantegna S., Cravotto G., Fubini B. (2007) The combination of oxalic acid with power ultrasound fully degrades chrysotile asbestos fibres. J. Environ. Monit., 10, 1064-6.

Turci F., Colonna M., Tomatis M., Mantegna S., Cravotto G., Fubini B. (2011a) New detoxification processes for asbestos fibers in the environment. J. Toxicol. Environ. Health A., 73, 368-77.

Turci F., Tomatis M., Lesci I.G., Roveri N., Fubini B. (2011b) The iron-related molecular toxicity mechanism of synthetic asbestos nanofibres: A model study for high-aspect-ratio nanoparticles. Chem. Eur. J. 17, 350-358.

Turci F., Tomatis M., Pacella A (2017) Surface and bulk properties of mineral fibres relevant to toxicity. In: A.F. Gualtieri (Ed.) “Mineral fibres: crystal chemistry, chemical–physical properties, biological interaction and toxicity”. European Mineralogical Union, London, pp. 171–214.

Van Gosen B.S., Lowers H.A., Sutley S.J., Gent C.A. (2004) Using the geologic setting of talc deposits as an indicator of amphibole asbestos content. Environ. Geol. 45, 920-939.

Van Oss C.J., Naim J.O., Costanzo P.M., Giese Jr. R.F., Wu W., Sorling A.F. (1999) Impact of different asbestos species and other mineral particles on pulmonary pathogenesis: clay. Clay Min. 47, 697–707.

Vermaas F. (1952) The amphibole asbestos of South Africa. T. Geol. Soc. South Africa 55, 199-232.

Vignaroli G., Ballirano P., Belardi G., Rossetti F. (2014) Asbestos fibre identification vs. evaluation of asbestos hazard in ophiolitic rock mélanges, a case study from the Ligurian Alps (Italy). Environ. Earth Sci. 72, 3679-3698.

Virta R.L. (1989) The Talc Industry-An Overview; U.S. Department of the Interior, Bureau of Mines: Washington, DC, USA, p. 30.

Vitale A.A., Bernatene E.A., Vitale M.G., and Pomilio A.B. (2016) New insights of the Fenton reaction using glycerol as experimental model. Effect of O_2, inhibition by Mg^{2+}, and oxidation state of Fe. J. Phys. Chem. A, 120, 28, 5435-5445.

Wagner J.C., Chamberlain M., Brown R.C., Berry G., Pooley F.D., Davies R., Griffiths D.M. (1982) Biological effects of tremolite. Br. J. Cancer 45, 352-360.

Witek J. and Kusiorowski R. (2017). Neutralization of cement-asbestos waste by melting in an arc-resistance furnace. Waste Manage. 69, 336-345.

Wittels M. (1952). The structural disintegration of some amphiboles. Amer. Mineral. 37, 28-36.

Yamamoto T., Kida A., Noma Y., Terazono A., Sakai S. (2016) Evaluation of thermally treated asbestos based on fiber number concentration determined by transmission electron microscopy. J. Mater. Cycles Waste Manage. 20, 214-222.

Young R.A. (1993) Introduction to the Rietveld method: In: R.A. Young (Ed.) “The Rietveld method”. Oxford University Press, pp. 1-38.

Supplementary material:
Tables

Table S1
List of reference structural data used in the present work in the Rietveld refinements.

Phase	Reference structural data
Crocidolite	Pacella et al. (2019)
Tremolite	Pacella et al. (2010)
Subcalcic diopside	McCallister et al. (1974)
Calcium-rich clinoenstatite	Clark et al. (1971)
Aegirine	Redhammer et al. (2006)
Cristobalite low	Downs and Palmer (1994)
Hematite	Finger and Hazen (1980)
Quartz	Le Page and Donnay (1976)

Table S2
Cell parameters and volume of tremolite and crocidolite fibres and agreement factors (as defined in Young, 1993) of the Rietveld refinement. For comparison purposes data of Pacella et al. (2010) for Maryland tremolite (RT P2010), Pacella et al (2019) for UICC crocidolite at RT (RT P2019), of Susta et al. (2018) for riebeckite (S2018) and of Oberti et al. (2018) for deprotonated riebeckite measured at RT (O2018 298KR) are reported.

	Tremolite			Crocidolite			
	RT P2010	Present work	RT P2019	650°C	800°C	S2018	O2018 298KR
R_{Bragg} (%)	2.55	1.03	0.50	0.49	0.91	-	-
R_{wp} (%)	2.21	2.61	2.61	3.51	4.17	-	-
R_p (%)	1.51	1.96	1.60	2.56	2.97	-	-
GoF	6.06	2.82	4.20	4.00	4.67	-	-
DWd	-	0.73	1.65	1.61	1.26	-	-
a (Å)	9.8538(2)	9.85210(7)	9.73511(19)	9.6167(2)	9.6322(3)	9.770(6)	9.6487(7)
b (Å)	18.0709(2)	18.07577(11)	18.0451(3)	17.8612(4)	17.8752(6)	18.080(10)	17.8994(4)
c (Å)	5.27903(6)	5.28106(3)	5.32892(8)	5.27885(10)	5.27873(14)	5.339(3)	5.2851(4)
β (Å)	104.738(1)	104.7483(5)	103.5158(12)	103.4770(16)	103.597(2)	103.599(13)	103.722(5)
Vol. (Å^3)	909.09(2)	909.488(10)	910.21(3)	881.76(3)	883.40(5)	916.6(9)	886.72(12)

		Tremolite		Crocidolite				
		RT P2010	Present work	RT P2019	650°C	800°C	S2018	O2018 298KR
T(1)	-O(7)	1.620(4)	1.617(2)	1.607(4)	1.615(5)	1.611(9)	1.6209(10)	1.624(3)
	-O(6)	1.650(6)	1.647(5)	1.646(7)	1.623(8)	1.642(13)	1.6279(12)	1.615(4)
	-O(1)	1.587(6)	1.585(4)	1.608(9)	1.640(12)	1.662(19)	1.6252(14)	1.611(3)
	-O(5)	1.650(5)	1.652(4)	1.611(9)	1.606(10)	1.620(16)	1.6268(11)	1.617(3)
<*T*(1)-O>		1.627	1.625	1.618	1.621	1.634	1.625	1.617
T(2)	-O(4)	1.579(5)	1.584(3)	1.586(8)	1.589(8)	1.657(14)	1.5996(12)	1.586(3)
	-O(5)	1.653(5)	1.647(3)	1.643(8)	1.641(9)	1.601(14)	1.6451(11)	1.642(4)
	-O(2)	1.615(6)	1.622(4)	1.599(10)	1.620(12)	1.64(2)	1.6254(14)	1.636(3)
	-O(6)	1.669(5)	1.677(3)	1.652(8)	1.659(10)	1.627(16)	1.6567(11)	1.645(3)
<*T*(2)-O>		1.629	1.633	1.620	1.627	1.631	1.632	1.627
M(1)	-O(3) x2	2.077(4)	2.086(2)	2.098(7)	1.954(8)	1.950(14)	2.1331(12)	1.942(3)
	-O(1) x2	2.074(5)	2.066(3)	2.089(8)	2.043(11)	2.047(16)	2.1087(13)	2.058(3)
	-O(2) x2	2.081(5)	2.089(3)	2.128(7)	2.046(8)	2.118(13)	2.1125(12)	2.096(3)
<*M*(1)-O>		2.077	2.080	2.105	2.014	2.038	2.118	2.032
M(2)	-O(4) x2	2.028(7)	2.026(3)	1.911(7)	1.891(7)	1.848(13)	1.9219(11)	1.911(3)
	-O(2) x2	2.074(6)	2.076(3)	2.045(9)	2.085(11)	2.061(17)	2.0371(12)	2.050(3)
	-O(1) x2	2.149(6)	2.134(3)	2.151(7)	2.197(8)	2.169(13)	2.1354(12)	2.152(3)
<*M*(2)-O>		2.084	2.079	2.036	2.058	2.026	2.031	2.038
M(3)	-O(1) x4	2.083(5)	2.100(2)	2.137(7)	2.132(8)	2.130(13)	2.1362(12)	2.162(3)
	-O(3) x2	2.059(6)	2.051(4)	2.121(11)	2.039(14)	2.07(2)	2.096(2)	2.047(5)
<*M*(3)-O>		2.075	2.084	2.132	2.101	2.109	2.123	2.124
<<*M*(1,2,3)-O>>		2.079	2.081	2.091	2.058	2.058	2.089	2.064
<<$\mathbf{r}^{M(1,2,3)}$>>*		0.723	0.725	0.738	0.696	0.697	0.735	0.704
M(4)	-O(4) x2	2.329(6)	2.340(3)	2.340(9)	2.382(10)	2.334(18)	2.3407(13)	2.399(3)
	-O(2) x2	2.394(6)	2.395(3)	2.422(9)	2.412(15)	2.33(2)	2.4319(14)	2.431(4)
	-O(6) x2	2.553(6)	2.550(3)	2.517(8)	2.450(15)	2.47(2)	2.4928(14)	2.469(4)
	-O(5) x2	2.775(6)	2.772(3)	2.896(8)	2.937(12)	2.909(18)	2.8994(14)	2.920(4)
<*M*(4)-O>		2.513	2.514	2.544	2.545	2.511	2.541	2.555

Table S3

Relevant bond distances (in Å) of Maryland tremolite and UICC crocidolite fibres. For comparison purposes data of Pacella et al. (2010) for Maryland tremolite (RT P2010), Pacella et al (2019) for UICC crocidolite at RT (RT P2019), of Susta et al. (2018) for riebeckite (S2018) and of Oberti et al. (2018) for deprotonated riebeckite measured at RT (O2018 298KR) are reported.
* Calculated as in Table 7 of Hawthorne and Oberti (2007).

Table S4
Site scattering (*s.s.*) at A, B and C sites from Rietveld refinement and Fe^{2+}/Fe^{3+} partition from $<r^M>$ of Maryland tremolite. Data of Pacella et al. (2010) are reported for comparison (RT P2010).

	s.s. (e^-)		Fe^{2+}/Fe^{3+} partition from $<r^M>$	
Site	RT P2010	Present work	RT P2010	Present work
C				
M(1)	25.97(14)	25.88(7)	$[Mg_{1.82}Fe^{2+}_{0.18}]$	$[Mg_{1.87(1)}Fe^{3+}_{0.03}Fe^{2+}_{0.10}]$
M(2)	25.49(14)	25.27(7)	$[Mg_{1.75}Fe^{3+}_{0.08}Fe^{2+}_{0.17}]$	$[Mg_{1.91(1)}Fe^{3+}_{0.06}Fe^{2+}_{0.03}]$
M(3)	13.27(11)	13.14(5)	$[Mg_{0.91}Fe^{2+}_{0.09}]$	$[Mg_{0.919(4)}Fe^{2+}_{0.081}]$
$\Sigma_{M(1)+M(2)+M(3)}$	**64.7(4)**	**64.29(19)**	**$[Mg_{4.48}Fe^{3+}_{0.08}Fe^{2+}_{0.44}]$**	**$[Mg_{4.70(2)}Fe^{3+}_{0.09}Fe^{2+}_{0.21}]$**
B				
M(4)	39.36(16)	39.83(8)	$Ca_{1.99}Mn_{0.02}Na_{0.01}$	$Ca_{1.992(4)}$
A	-	0.38(5)	-	$Na_{0.035(4)}$

Table S5
Cell parameters of the two pyroxenes produced by the breakdown of tremolite from Maryland.

Phase	*a* (Å)	*b* (Å)	*c* (Å)	*β* (Å)	*Vol.* ($Å^3$)
Subcalcic diopside	9.7283(4)	8.9030(3)	5.25101(19)	106.617(2)	435.80(3)
Calcium-rich clinoenstatite	9.6885(8)	8.8828(7)	5.2158(4)	108.709(8)	425.15(6)

Table S6

Cell parameters of cristobalite occurring during the different thermal treatments. Reference data (B&D97) of Butler and Dyson (1997) are reported for comparison.

Sample	*a* (Å)	*c* (Å)	*Vol.* (Å^3)
Tremolite 1200°C	5.0010(15)	6.988(4)	174.77(14)
Crocidolite 800°C	5.0515(13)	7.016(3)	179.03(12)
Crocidolite 1000°C	5.0155(11)	7.037(3)	177.01(12)
α-cristobalite B&D97	4.973	6.924	171.24
α'-cristobalite B&D97	5.01	7.00	175.70

Figures

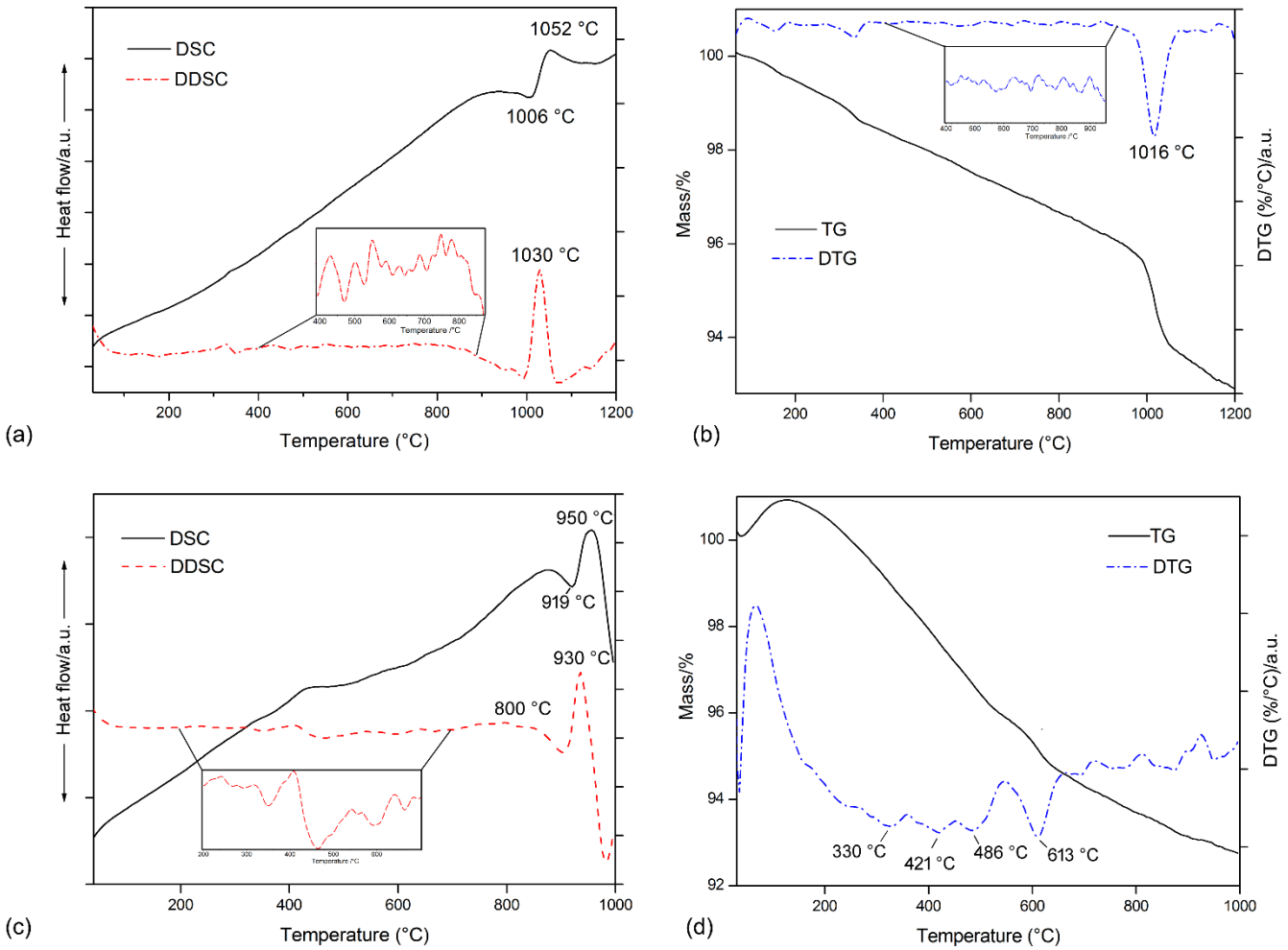

Fig. S1. Calorimetric and thermogravimetric analysis of tremolite (a) and (b) and crocidolite (c) and (d). Differential scanning calorimetry (DSC) and derivative differential scanning calorimetry (DDSC) curves of tremolite (a) and crocidolite (c). Inset: zoom of DDSC curves. Thermogravimetry (TG) and derivative thermogravimetry (DTG) curves of tremolite (c) and crocidolite (c). Inset: zoom of DTG curves.

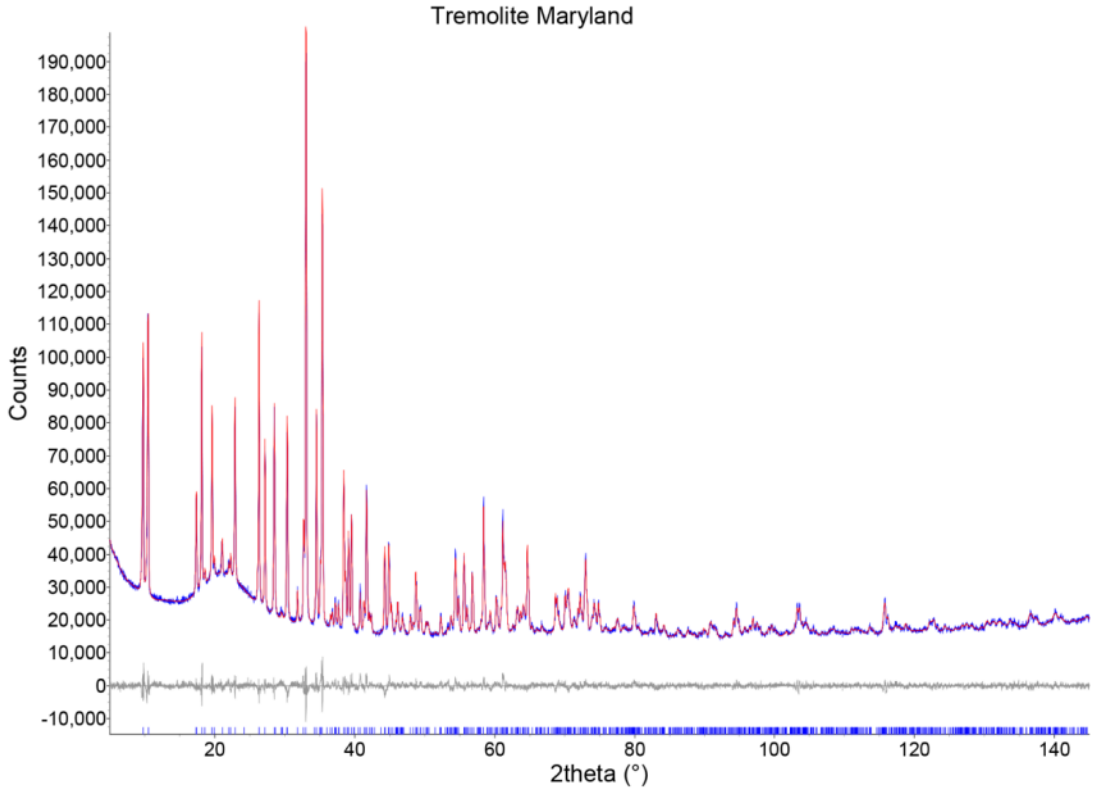
Tremolite Maryland
Counts
190,000
180,000
170,000
160,000
150,000
140,000
130,000
120,000
110,000
100,000
90,000
80,000
70,000
60,000
50,000
40,000
30,000
20,000
10,000
0
-10,000
20
40
60
80
100
120
140
2theta (°)

(a)

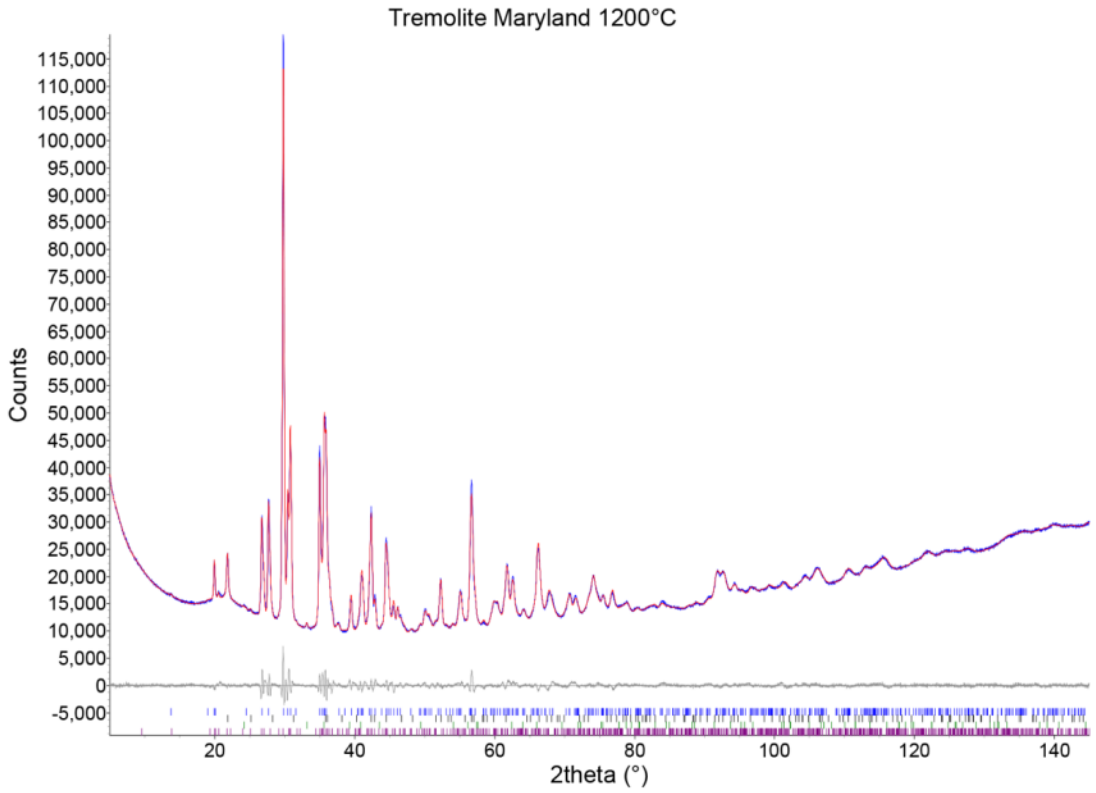
Tremolite Maryland 1200°C
Counts
115,000
110,000
105,000
100,000
95,000
90,000
85,000
80,000
75,000
70,000
65,000
60,000
55,000
50,000
45,000
40,000
35,000
30,000
25,000
20,000
15,000
10,000
5,000
0
-5,000
20
40
60
80
100
120
140
2theta (°)

b)

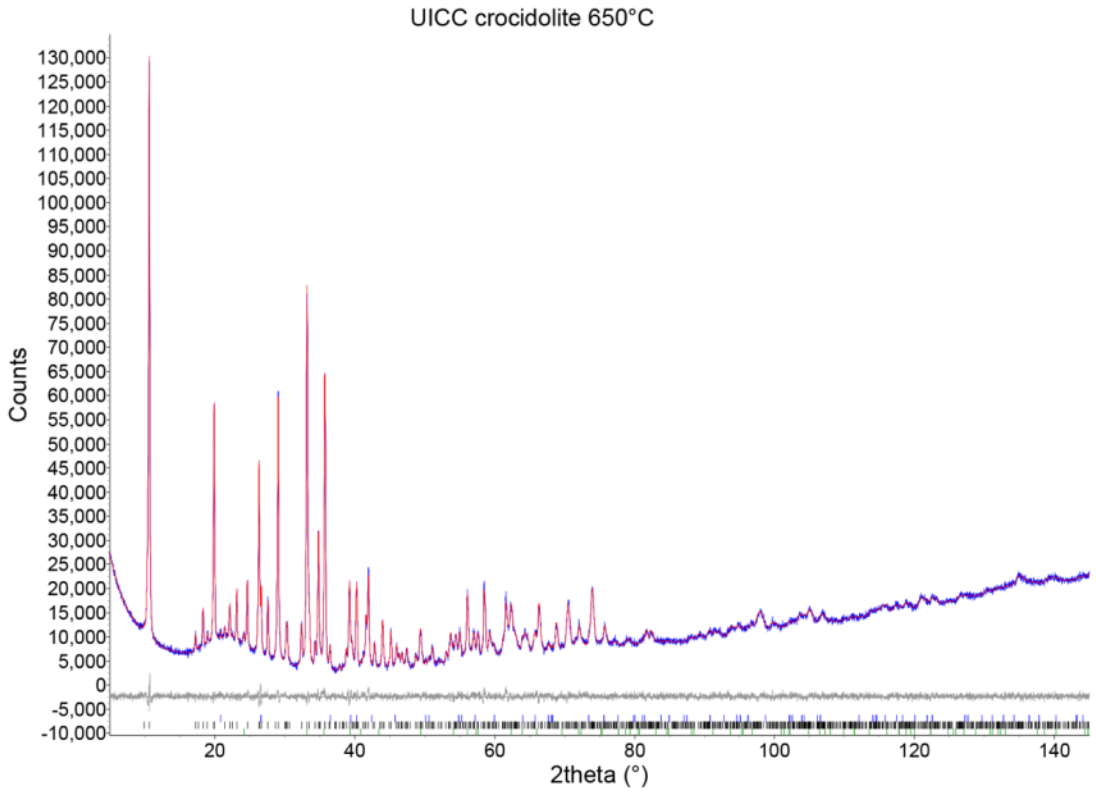
UICC crocidolite 650°C
Counts
130,000
125,000
120,000
115,000
110,000
105,000
100,000
95,000
90,000
85,000
80,000
75,000
70,000
65,000
60,000
55,000
50,000
45,000
40,000
35,000
30,000
25,000
20,000
15,000
10,000
5,000
0
-5,000
-10,000
20
40
60
80
100
120
140
2theta (°)

(c)

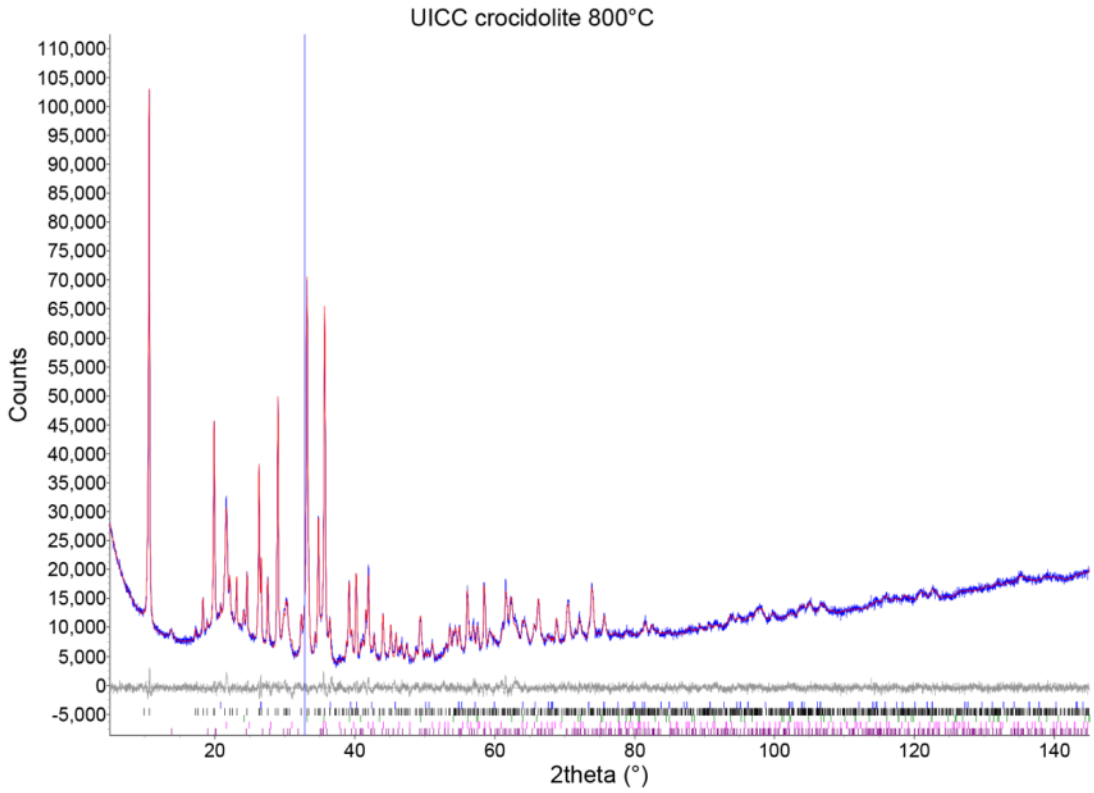
UICC crocidolite 800°C
Counts
110,000
105,000
100,000
95,000
90,000
85,000
80,000
75,000
70,000
65,000
60,000
55,000
50,000
45,000
40,000
35,000
30,000
25,000
20,000
15,000
10,000
5,000
0
-5,000
20
40
60
80
100
120
140
2theta (°)

(d)

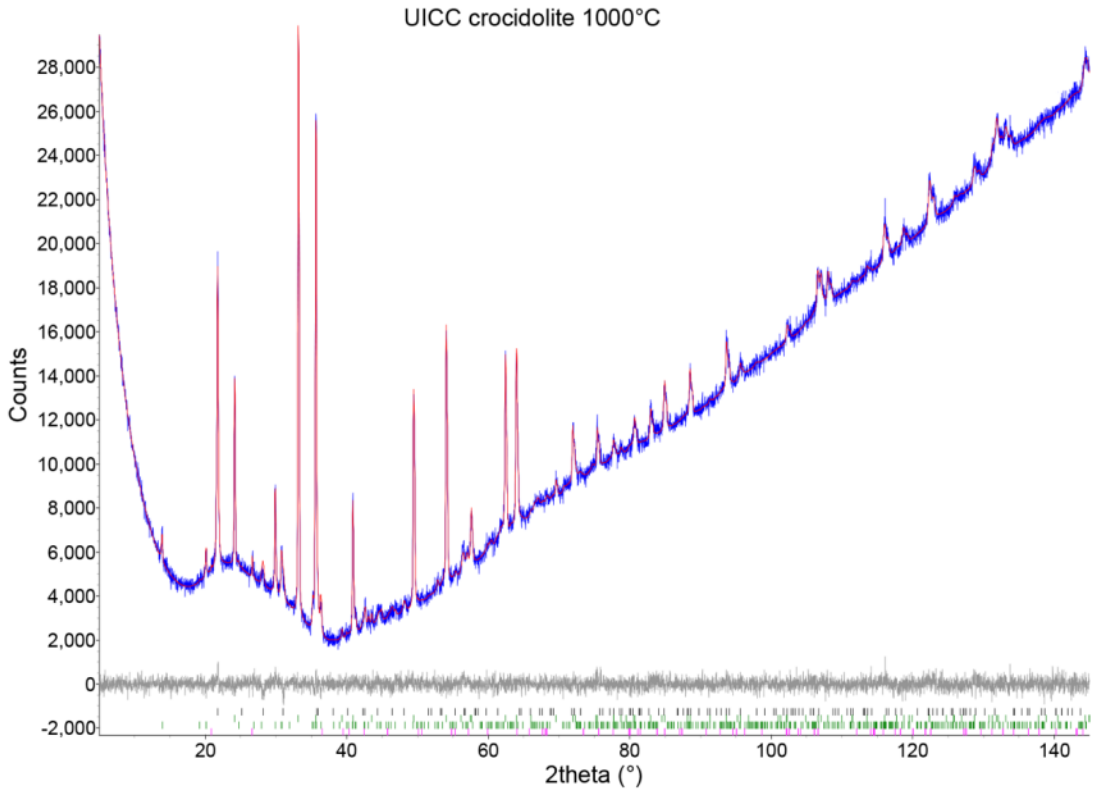

(e)

Fig. S2. Conventional Rietveld plots of (a) tremolite form Maryland; (b) tremolite from Maryland heated at 1200°C; (c) UICC crocidolite heated at 650°C; (d) UICC crocidolite heated at 800°C; (e) UICC crocidolite heated at 1000°C. Blue dots: experimental pattern; continuous red line: calculated pattern; continuous grey line: difference plot. Vertical bars represent the position of calculated Bragg reflection of the various phases occurring in the samples.

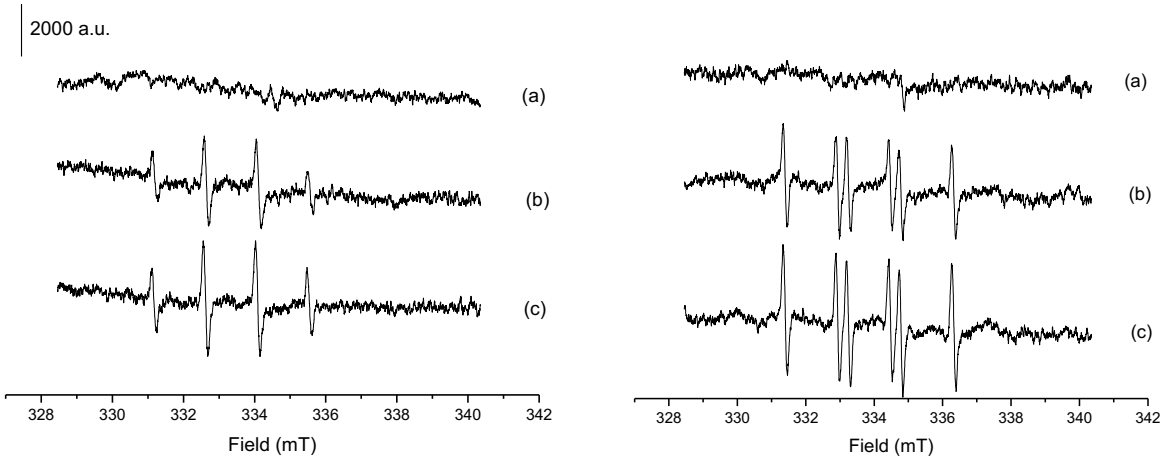

Fig. S3. Free radical release by breakdown products of UICC crocidolite: a) cristobalite, b) aegirine, and c) hematite. EPR spectra of A) $[DMPO\text{-}OH]^{\bullet}$ and B) $DMPO\text{-}COO^{-}]^{\bullet}$. Data reported refer to the maximum intensity of the EPR spectra recorded for each sample.